THE RAPID DEPLOYMENTS TO WILDFIRES EXPERIMENT (RaDFIRE)

Observations from the Fire Zone

Craig B. Clements, Neil P. Lareau, David E. Kingsmill, Carrie L. Bowers, Chris P. Camacho, Richard Bagley, and Braniff Davis

Observations from within the fire environment during active wildfires highlight meteorological processes associated with fire–atmosphere interactions.

Wildfires are a high-impact societal problem for the western United States and other fire-prone regions through threats to life and property, damage to natural resources, and degraded human health resulting from smoke. In addition, fire suppression costs strain federal, state, and local resources. For example, in the 1990s, the total annual fire suppression costs for the United States averaged ~$453 million (U.S. dollars) per year, and from 2006 to 2016, costs climbed to more than $1.53 billion per year [National Interagency Fire Center (NIFC); available at www.nifc.gov/fireInfo/fireInfo_documents/SuppCosts.pdf]. Contributing to these increasing costs is the increase in both the frequency and the spatial extent of wildfires because of climate change and other anthropogenic influences, such as the expansion of the wildland–urban interface. This trend is expected to continue over the coming decades (Westerling et al. 2006; Dennison et al. 2014; Flannigan et al. 2009; Barbero et al. 2015; Abatzoglou and Williams 2016).

While a warming climate may set the stage for worsening fire conditions, each fire ultimately responds to the nexus of fuels, terrain, and weather. Terrain is a fixed factor, and fuels are typically seasonally cured (though the dryness of fine fuels can vary at short time scales), whereas variable meteorological conditions can have profound effects on fire development (Werth 2011). In addition to weather factors (e.g., synoptic-scale systems, fronts, and thunderstorm outflows), fires also produce their own circulations, which can subsequently feed back on fire behavior.

AFFILIATIONS: Clements, Lareau, Bowers, Camacho, Bagley, and Davis—Fire Weather Research Laboratory, Department of Meteorology and Climate Science, San José State University, San Jose, California; Kingsmill—Cooperative Institute for Research in Environmental Sciences, University of Colorado Boulder, Boulder, Colorado
CORRESPONDING AUTHOR: Craig B. Clements, craig.clements@sjsu.edu

The abstract for this article can be found in this issue, following the table of contents.
DOI:10.1175/BAMS-D-17-0230.1

In final form 14 June 2018

THE RAPID DEPLOYMENTS TO WILDFIRES EXPERIMENT (RaDFIRE)

Observations from the Fire Zone

Craig B. Clements, Neil P. Lareau, David E. Kingsmill, Carrie L. Bowers, Chris P. Camacho, Richard Bagley, and Braniff Davis

Observations from within the fire environment during active wildfires highlight meteorological processes associated with fire–atmosphere interactions.

Wildfires are a high-impact societal problem for the western United States and other fire-prone regions through threats to life and property, damage to natural resources, and degraded human health resulting from smoke. In addition, fire suppression costs strain federal, state, and local resources. For example, in the 1990s, the total annual fire suppression costs for the United States averaged ~$453 million (U.S. dollars) per year, and from 2006 to 2016, costs climbed to more than $1.53 billion per year [National Interagency Fire Center (NIFC); available at www.nifc.gov/fireInfo/fireInfo_documents/SuppCosts.pdf]. Contributing to these increasing costs is the increase in both the frequency and the spatial extent of wildfires because of climate change and other anthropogenic influences, such as the expansion of the wildland–urban interface. This trend is expected to continue over the coming decades (Westerling et al. 2006; Dennison et al. 2014; Flannigan et al. 2009; Barbero et al. 2015; Abatzoglou and Williams 2016).

While a warming climate may set the stage for worsening fire conditions, each fire ultimately responds to the nexus of fuels, terrain, and weather. Terrain is a fixed factor, and fuels are typically seasonally cured (though the dryness of fine fuels can vary at short time scales), whereas variable meteorological conditions can have profound effects on fire development (Werth 2011). In addition to weather factors (e.g., synoptic-scale systems, fronts, and thunderstorm outflows), fires also produce their own circulations, which can subsequently feed back on fire behavior.

AFFILIATIONS: Clements, Lareau, Bowers, Camacho, Bagley, and Davis—Fire Weather Research Laboratory, Department of Meteorology and Climate Science, San José State University, San Jose, California; Kingsmill—Cooperative Institute for Research in Environmental Sciences, University of Colorado Boulder, Boulder, Colorado
CORRESPONDING AUTHOR: Craig B. Clements, craig.clements@sjsu.edu

The abstract for this article can be found in this issue, following the table of contents.
DOI:10.1175/BAMS-D-17-0230.1

In final form 14 June 2018

These fire–atmosphere interactions may include the development of convective plumes, fire-induced inflow winds, and smoke-radiative effects (Potter 2012).

Wildfire convective plumes link fire heat and moisture emissions to vertical and horizontal atmospheric circulations (Viegas 1998). Fire-induced circulations have also been associated with surges in fire spread (Coen et al. 2004) and also modulate smoke transport and injection height (Penner et al. 1992; Fromm and Servranckx 2003; Damoah et al. 2004). While the complex dynamics of wildfire plumes have long been identified as an important component of fire–atmosphere interaction (Byram 1959; Countryman 1971; Rothermel 1991), there is a paucity of quantitative field studies of these pyroconvective dynamics.

Vorticity in wildfire convective plumes impacts plume rise, fire propagation, and fire intensity (McRae and Flannigan 1990; Forthofer and Goodrick 2011; Potter 2012). Types of in-plume vorticity include counterrotating vortex pairs, whole column (vertical axis) vorticity, and horizontal axis plume edge vortices. Anecdotal, photographic, and computer-simulated evidence for these vortical structures is widely available (McRae and Flannigan 1990; Cunningham et al. 2005; Umscheid et al. 2006; Seto and Clements 2011), whereas detailed quantified observations are not. Banta et al. (1992), for example, provided direct measurements (with lidar and radar) of counterrotating vortex pairs and whole column rotation, but how these single instance observations compare to the scale and intensity of vortical structures in other fires is not known.

Beyond vortical structures, fires are also known to produce strong updrafts and horizontal inflow. Using infrared video analyses of crown fires, Clark et al. (1996) derived inflow velocities of ~5–15 m s^{-1}, updrafts up to 30 m s^{-1}, and downdrafts of ~10–20 m s^{-1}. Similarly, Coen et al. (2004) estimated updrafts on the order of 20–30 m s^{-1} near the base of one wildfire convective plume. The horizontal and vertical extent of these inflows and updrafts has not, however, been systematically observed across a broad sample of fires. It is not known, for example, how far outward from a wildfire convective plume inflow winds can be expected to extend.

The factors modulating smoke injection height also remain poorly understood and underobserved. Satellite observations provide observational context, indicating that only a small fraction (4%–12%) of smoke plumes inject smoke above the planetary boundary layer (Kahn et al. 2008; Val Martin et al. 2010) and that fire intensity (measured as fire radiative power) modulates the final injection height (Val Martin et al. 2012; Peterson et al. 2015). Yet process-level observations detailing how and under what conditions plume interactions with wind shear and temperature stratification affect plume rise and smoke detrainment are not typically available. Fires may modify the structure of the planetary boundary layer by reducing the insolation beneath detrained smoke layers (Robock 1988, 1991; Penner et al. 1992). Thus, stable layers and mixing heights near fires may differ from those resolved by forecast models and observed by regional radiosonde networks. These observational deficits, coupled with uncertainties in plume-rise models, led Val Martin et al. (2012) to conclude that direct field measurements of fire and smoke plume properties are required to produce the next major advances in plume-rise modeling.

While pyrocumulus (pyroCu) are relatively common, pyrocumulonimbus (pyroCb) have been linked to stratospheric smoke injection (Fromm and Servranckx 2003; Fromm et al. 2006, 2010), highly polluted cloud compositions (Andreae et al. 2004; Rosenfeld et al. 2007), and both in-cloud and positive polarity lightning (Lang and Rutledge 2006; Lang et al. 2014). The sensitivity of pyroCb to variations in aerosol loading, sensible heat flux, and water vapor have been simulated with dynamical models (Trentmann et al. 2006; Luderer et al. 2006, 2009) and the environmental conditions favoring pyroCb development have recently been examined (Peterson et al. 2017). However, observations of the internal structure and dynamics of these plumes are largely unavailable and pyroCu/pyroCb feedbacks on fire propagation are not yet known.

Meteorological observations near wildfires are rare, especially compared to the established observational record for other atmospheric processes (e.g., convective storms). This observational deficit likely stems from the considerable logistical and safety challenges associated with sampling in the near-fire environment (Viegas 1998), and therefore, there is a need for obtaining observations from within the near-fire environment. The goals of this paper are twofold. First, it summarizes the design and execution of the Rapid Deployments to Wildfires Experiment (RaDFIRE) campaign, fire-selection and deployment strategies, observational tools, and integration with fire management. Second, it highlights some of the seldom documented aspects of fire–atmosphere interactions observed during the campaign.

DEPLOYMENT STRATEGY TO WILDFIRE INCIDENTS.

To observe wildfire convective plume dynamics and other fire–atmosphere interactions during active wildfires, a rapid-response deployment

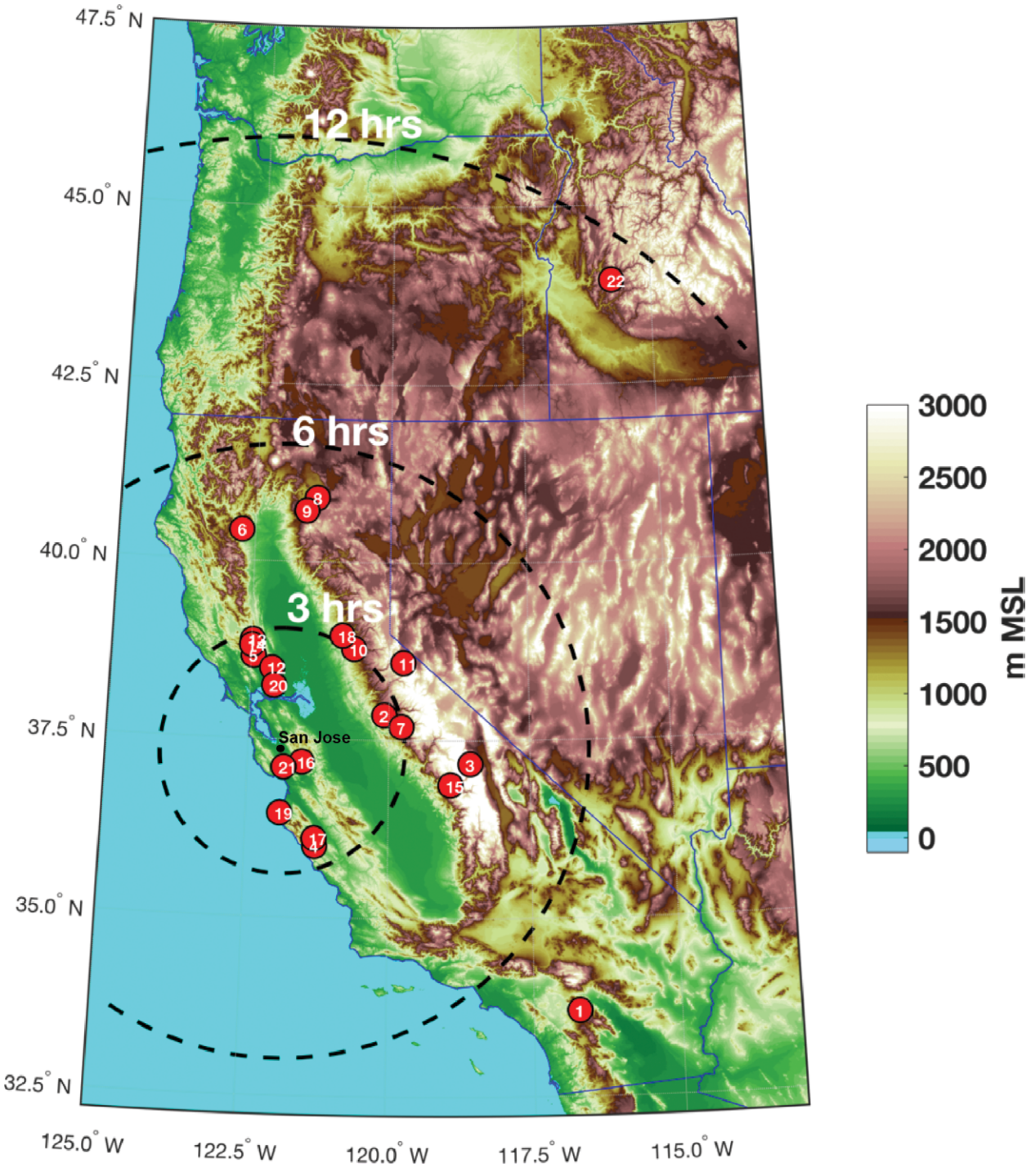

Fig. 1. Map showing RaDFIRE deployments in the western United States. Range rings indicate approximate response times for wildfire incidents from San Jose, CA. Numbers in each circle indicate fire number as listed in Table 1.

strategy was utilized. This strategy required evaluation of individual wildfires for their research potential based on expected spread patterns, weather conditions, and societal impacts. Spread patterns, for example, were estimated from forecast wind and weather patterns, in conjunction with the inspection of the terrain and vegetation for regions conducive to unimpeded fire growth within a deployment window. Deployment decisions were based partly on access considerations, especially the availability of roads and clear lines of sight. Deployments were limited to wildfires within the western United States and within a maximum driving or travel time of 12 h from the RaDFIRE base at San José State University (SJSU) (Fig. 1). All

THE INCIDENT COMMAND SYSTEM

The Incident Command System (ICS) is a standardized system designed to allow emergency responders to adapt management strategies to a variety of incidents with varying levels of complexity. Command of the incident falls to the incident commander (IC) or unified command. Under the incident commander are the command staff (safety, liaison, and information) and four additional functional sections: operations, planning, logistics, and finance and administration. These sections have areas under their purview. The ICS is structured so that only the sections that are needed are staffed and personnel can be added or released as needed.

The operations section is responsible for all operations pertaining to the primary mission of the incident. The planning section is responsible for gathering, assessing, and distributing information related to the incident operations, as well as the preparation of the incident action plan (IAP). It is under the planning section that RaDFIRE generally operates when assigned to an incident, specifically under the guidance of either the incident meteorologist or the fire behavior analyst. Logistics staff address the needs of responders by providing the facilities, services, and equipment needed for an effective response. The finance and administration section is responsible for all cost and administrative needs related to the incident (www.fema.gov/incident-command-system-resources).

When a fire is first detected, the agencies with jurisdiction respond. The first responder on the scene assumes the position of IC until an individual with more training or more appropriate jurisdiction arrives and takes over. The IC directs suppression strategies, provides for responder and public safety, and orders more resources as necessary. A fire may be suppressed or controlled within one operational period, or it may continue into days, weeks, or even months.

As a fire increases in size and/or complexity, the IC divides the fire into functional or area divisions so that he or she can decrease the number of people directly under his or her command. As the fire decreases in complexity, the IC can release resources and combine divisions. In this way, the ICS can be expanded or shrunk according to need.

Different fires may require different objectives. The primary objective across all incidents is to ensure the safety of the public and the responders. Additional objectives might include the protection of property or other valuables at risk, limiting the spread of a fire to a specified area, or allowing the fire to burn a specified area.

deployments were in California with the exception of a single exploratory airborne campaign that used the University of Wyoming King Air (UWKA) to observe plume structures during a large wildfire in Idaho (ID).

Access to wildfire incidents is generally limited to fire-line-qualified personnel (i.e., firefighters and forest managers). This requirement is the foundation of the National Incident Command System (NICS; see sidebar) and limits a research team's proximity to the fire front. To overcome this access constraint, all members of the SJSU research team receive annual fire line training following the standards set by the National Wildfire Coordinating Group. Team members who respond to wildfire incidents are qualified as either "Firefighter Type II" or "Technical Specialists."

SJSU has a formal memorandum of understanding with the Tahoe National Forest to maintain status in the federal Resource Ordering and Status System (ROSS; http://famit.nwcg.gov/applications/ROSS) in order to be requested for a wildfire incident. ROSS "tracks all tactical, logistical, service and support resources mobilized by the incident dispatch community." Generally, the team can be requested in two ways. First, someone at the incident determines that there is a need for the team's observational capability and calls the team to inquire about its availability. Second, when the team determines that an incident is of scientific interest, it may deploy preemptively. In this circumstance, SJSU team members reach out to personnel on the fire and ask to be requested. If a formal request is not granted, the team aborts deployment. When the team is integrated with an incident, members must first go through the incident check-in procedure during which the team is provided logistical information, including maps and the Incident Action Plan. Additionally, the SJSU team radios are synchronized with the incident frequencies. The team will then report to either the NWS incident meteorologist (IMET), the fire behavior analyst (FBAN), or the planning section chief for current fire information and guidance on where to stage the team and the instruments.

There were times that the team deployed to wildfire incidents but was not officially assigned to the incident. In these cases, the team made measurements from a nearby highway, in designated media locations, or at other locations as indicated by fire personnel. These locations, while sometimes not ideal, provided a safe setting for observations.

METHODS AND EXPERIMENTAL DESIGN.

Mobile profiling system. The Fire Weather Research Laboratory operates a rapid-response mobile atmospheric profiling system—the California State University Mobile Atmospheric Profiling System (CSU-MAPS; Clements and Oliphant 2014). It includes a scanning Doppler lidar, microwave profiler, radiosonde system, and automated weather station. The system was designed for boundary layer profiling of the near-fire

environment and to measure smoke plume dynamics. The CSU-MAPS can be operated in either fixed or mobile profiling configurations, enabling rapid response and adaptive measurement strategies. For example, the lidar can be operated while the vehicle is in motion, thereby reducing the startup time if the CSU-MAPS is moved to a different location.

A key component of the CSU-MAPS is the Halo Photonics 1.5-μm scanning Doppler lidar with a range of 9,600 m and a range gate resolution of 18 m (Pearson et al. 2009). The lidar records 1) the attenuated backscatter coefficient and 2) the Doppler velocity. The attenuated backscatter coefficient (hereafter backscatter) is sensitive to micrometer-sized aerosol, including forest fire smoke, which typically exhibits a lognormal particle number distribution with a peak near 0.13 μm and a long tail extending toward coarser particles (Radke et al. 1990, 1991; Banta et al. 1992; Reid and Hobbs 1998; Reid et al. 2005). Banta et al. (1992) showed that infrared lidar backscatter from smoke plumes is primarily from 0.5–2-μm particles, though the contribution from the numerous smaller particles and the sparse larger particles also contributes to the total backscatter. As such, we postprocessed the data as the $\log_{10}$ of the backscatter and interpreted the results as being proportional to the smoke concentrations. In our observations, smoke backscatter typically ranged from -6 to -4 m^{-1} sr^{-1}, and lower values (i.e., -7 m^{-1} sr^{-1}) corresponded to "clear air." The lidar beam sometimes attenuated from heavy aerosol loads in deep plumes and rapidly attenuated with high liquid content of clouds.

The Doppler velocity data were used to investigate aspects of the airflow in and around the convective plumes and within the ambient convective boundary layer (CBL). The velocity data have a precision of ~0.03 m s^{-1} and a range of ±19 m s^{-1}. The velocities reported here, and in other RaDFIRE papers (Lareau and Clements 2015, 2016, 2017), typically result from the motion of airborne smoke and ash particles. Velocity returns are often not available outside of the smoky regions because of the low signal-to-noise ratio (SNR) in pristine mountain environments.

The lidar was operated primarily in a range–height indicator (RHI) scanning mode, with scans centered on the upright portions of the wildfire plumes. Typical RHI sweeps cover ~75° in elevation in ~30 s, providing a beam-to-beam resolution of 41 m at a range of 2 km. Velocity–azimuth display (VAD) scans were also occasionally interspersed with the RHI scans to retrieve the vertical profile of the horizontal

Table 1. Key UWKA instrumentation for RaDFIRE.

Instruments	Characteristics/capabilities
	In situ
Standard flight-level parameters	Navigation (e.g., 3D position, ground speed, airspeed, orientation), winds (e.g., horizontal wind speed and direction, vertical air velocity), state (e.g., pressure, temperature, water vapor)
Droplet Measurement Technologies (DMT) LWC100	Liquid water content for cloud droplets up to ~50 μm
Gerber PVM100	Liquid water content for cloud droplets up to ~60 μm
SkyTech Nevzorov	Total water content and liquid water content
DMT CDP	Size distribution of cloud droplets from 2–50 μm
DMT CIP	Two-dimensional particle imagery with optical-array width of 1.6 mm and resolution of 25 μm; derivation of particle shapes and size distributions
Stratton Park Engineering Company (SPEC) 2DS	Two-dimensional stereographic particle imagery with optical array widths of 1.28 mm and resolutions of 10 mm; derivations of particle shapes and size distributions
Particle Measuring Systems (PMS) 2DP	Two-dimensional particle imagery with optical-array width of 6.4 mm and resolution of 200 μm; derivation of particle shapes and size distributions
	Remote sensing
WCR	95-GHz cloud radar with upward, downward, and down-forward beams; output fields of reflectivity, radial velocity, and spectrum width at spatial resolutions of a few tens of meters
WCL	351-nm cloud lidar with downward beam; output fields of backscatter coefficient and linear depolarization ratio at spatial resolutions of a few meters
Heitronics KT-15.85	Downward-pointing radiative thermometer sensitive to the 9.6–11.5-μm infrared radiation band; estimate of surface temperature
Video camera	Forward and downward visual imagery

Table 2. List of fire deployments.

No.	Incident name	State	Location	Start date	Containment date	Total hectares burned	RADFIRE obs dates	Hectares burned during obs	Obs type	Relevant details
1	Mountain fire	CA	33.705°N, 116.726°W	15 Jul 2013	25 Aug 2013	11,141	20 Jul 2013	0	Lidar, radiosonde, microwave profiler	
2	Rim fire	CA	37.857°N, 120.086°W	17 Aug 2013	24 Oct 2013	104,131	21 Aug 2013 23 Aug 2013 26 Aug 2013 29 Aug 2013 8–9 Sep 2013	15,232 8,094 4,532 2,630 548	Lidar, radiosonde, microwave profiler	PyroCu
3	Shirley fire	CA	35.717°N, 118.555°W	13 Jun 2014	15 Jul 2014	1,030	16–17 Jun 2016	181	Lidar, microwave profiler	
4	Stoney fire	CA	36.006°N, 121.275°W	19 Jun 2014	21 Jun 2014	1,959	20 Jun 2014		Lidar, microwave profiler	Fire whirl
5	Butts fire	CA	38.664°N, 122.454°W	1 Jul 2014	9 Jul 2014	1,740	2 Jul 2014	55	Lidar, radiosonde, microwave profiler	
6	Bully fire	CA	40.431°N, 122.751°W	11 Jul 2014	26 Jul 2014	5,124	11–12 Jul 2014	1,186	Lidar, radiosonde, microwave profiler	
7	El Portal fire	CA	37.691°N, 119.778°W	26 Jul 2014	5 Aug 2014	1,898	28–30 Jul 2016	369	Lidar, radiosonde, microwave profiler	
8	Bald fire	CA	40.901°N, 121.368°W	30 Jul 2014	12 Aug 2014	16,080	2–3 Aug 2016	8,636	Lidar, radiosonde, microwave profiler	PyroCu
9	Eiler fire	CA	40.72°N, 121.562°W	31 Jul 2014	25 Aug 2014	13,118	2–3 Aug 2016	9,996	Lidar, radiosonde, microwave profiler	PyroCu
10	King fire	CA	38.782°N, 120.64°W	13 Sep 2014	9 Oct 2014	39,545	16–17 Sep 2014	13,723	Lidar, radiosonde, microwave profiler	
11	Washington fire	CA	38.592°N, 119.752°W	19 Jun 2015	17 Aug 2015	7,199	23–24 Jun 2015	>40	Lidar, radiosonde, microwave profiler	
12	Wragg fire	CA	38.499°N, 122.115°W	22 Jul 2015	5 Aug 2015	3,258	23 Jul 2015	1,174	Lidar, radiosonde	
13	Rocky fire	CA	38.886°N, 122.476°W	29 Jul 2015	14 Aug 2015	28,100	30 Jul 2015	2,104	Lidar, radiosonde	PyroCu
14	Jerusalem fire	CA	38.814°N, 122.487°W	9 Aug 2015	25 Aug 2015	10,165	13 Aug 2016	202	Lidar	

Table 2. Continued.

No.	Incident name	State	Location	Start date	Containment date	Total hectares burned	RADFIRE obs dates	Hectares burned during obs	Obs type	Relevant details
15	Rough fire	CA	36.874°N, 118.905°W	31 Jul 2015	5 Nov 2015	61,360	18–19 Aug 2015	2,955	Lidar, radiosonde	
16	Henry Coe control burn	CA	37.184°N, 121.534°W	19 Nov 2015	19 Nov 2015	255	19 Nov 2015	255	Lidar, radiosonde	Control burn
17	Coleman fire	CA	36.113°N, 121.289°W	4 Jun 2016	21 Jun 2016	1,020	6–7 Jun 2016	>40	Lidar, radiosonde	
18	Trailhead fire	CA	38.969°N, 120.854°W	28 Jun 2016	18 Jul 2016	2,285	30 Jun 2016	121	Mobile transect, lidar	
19	Soberanes fire	CA	36.461°N, 121.901°W	22 Jul 2016	12 Dec 2016	53,470	26 Jul 2016 11 Aug 2016	2,369 315	Mobile transect, lidar, radiosonde	
20	Cold fire	CA	38.525°N, 122.068°W	2 Aug 2016	12 Aug 2016	2,319	3 Aug 2016	243	Mobile transect, lidar	
21	Loma fire	CA	37.106°N, 121.853°W	26 Sep 2016	12 Dec 2016	1,811	26–28 Sep 2016	1,159	Mobile transect, lidar	
22	Pioneer fire	ID	43.95°N, 115.762°W	18 Jul 2016	4 Nov 2016	76,244	29 Aug 2016 30 Aug 2016	11,807 6,711	Lidar, radar (Wyoming King Air)	PyroCu, PyroCb

wind (Browning and Wexler 1968). Sector plan position indicator (PPI) scans were also conducted on some fires.

In addition to these traditional sampling techniques, mobile lidar observations were also conducted on seven fires. In these scans, the lidar was fixed in vertically staring mode while the truck was in motion, thereby providing time-and-space-resolved measurements of convective boundary layer and smoke layer structures near fires. As we show later, these data provide insights into the fire-modified environment.

UWKA. The UWKA was used as part of an exploratory aircraft campaign within the broader scope of RaDFIRE. The UWKA was equipped with a wide array of in situ and remote sensing instrumentation (Wang et al. 2012). The key instruments deployed on the aircraft during RaDFIRE are outlined in Table 1. The in situ sensors provided information about navigation (aircraft position, speed, and orientation), winds (horizontal and vertical), state parameters (pressure, temperature, and water vapor content), and various cloud physics characteristics (total water content, liquid water content, particle shapes, and size distributions). The primary remote sensing instrument was the W-band (95 GHz) Wyoming Cloud Radar (WCR), which provided reflectivity, radial velocity, and spectrum width along beams directed upward, downward, and down forward. Other remote sensors included the Wyoming Cloud Lidar (WCL) with downward-directed beams that provided backscatter coefficient and linear depolarization ratios, a downward-pointing infrared thermometer, and forward- and downward-pointing video cameras.

The fires. In total, the CSU-MAPS was deployed to 20 wildfires in California (CA) during the RaDFIRE campaign. The UWKA was deployed to one additional fire: the Pioneer fire in Idaho. Fire locations, fire dates, acreage burned, and other details are provided in Table 2 and Fig. 1. Typical deployment durations ranged from 12 h to 3 days.

Collectively, the sampled fires ranged from small short-lived fires producing relatively minor plumes confined to the lower

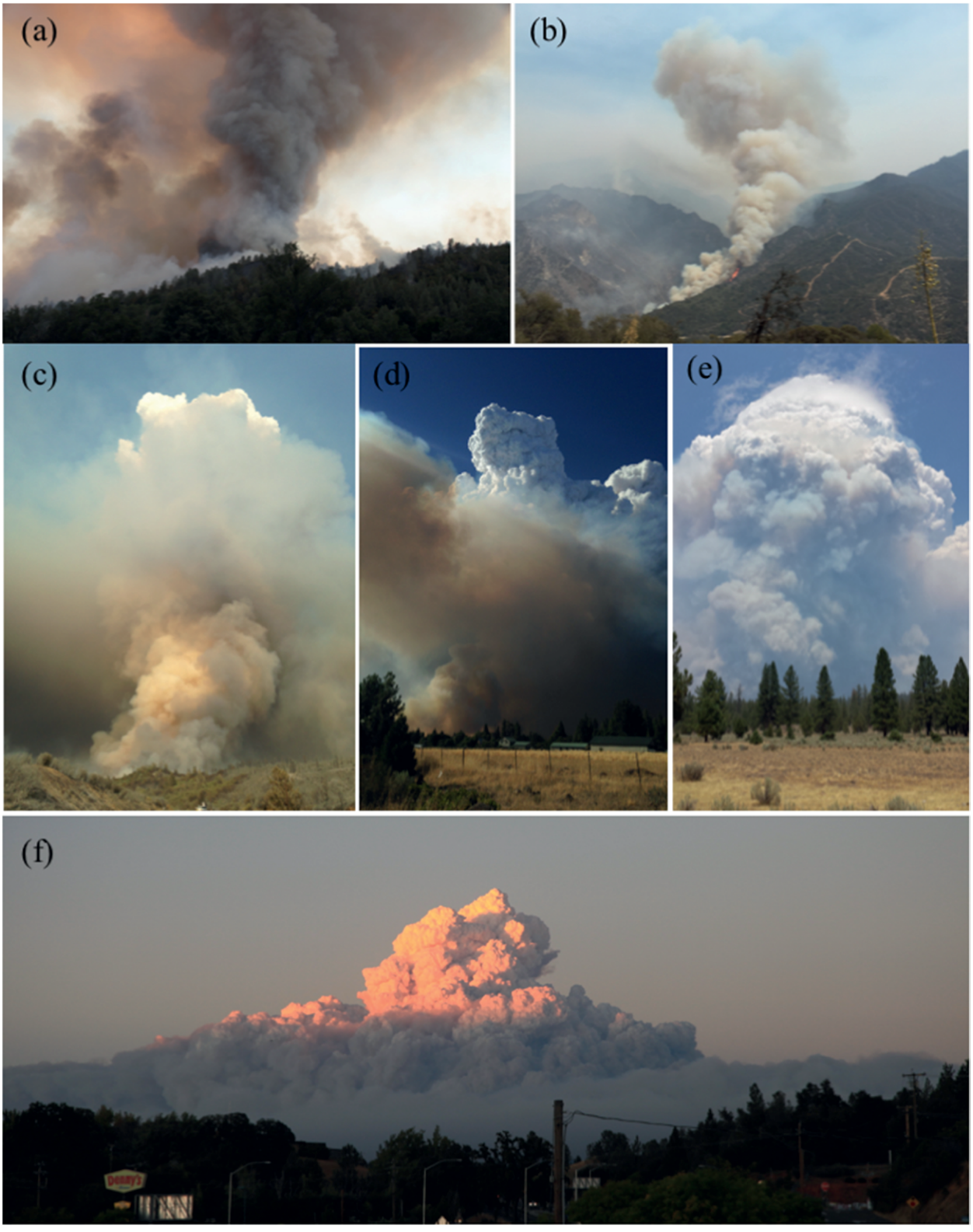

Fig. 2. Photos of wildfire plumes sampled during RaDFIRE. (a) Rotating column of Stoney fire, (b) Rough fire, (c) Rocky fire, (d) Eiler fire, (e) Bald fire, and (f) King fire.

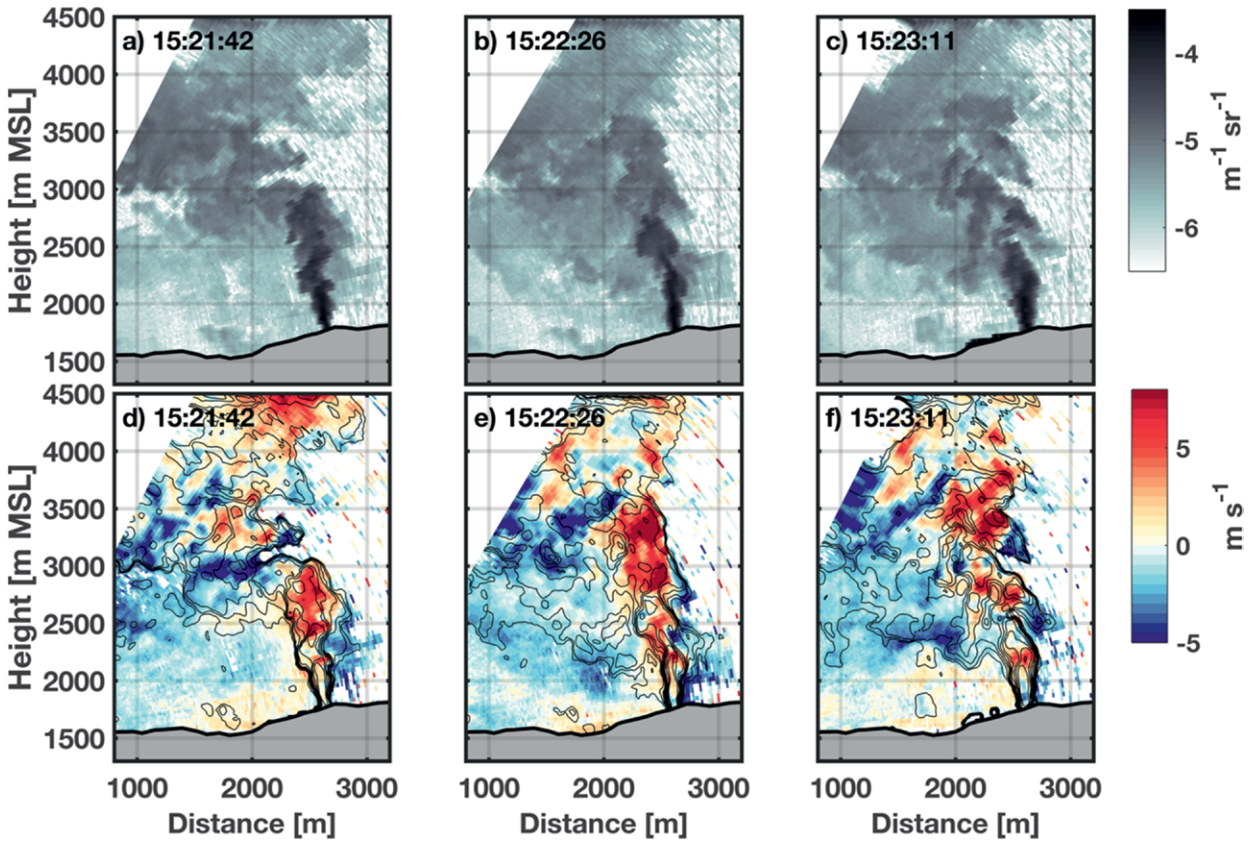

Fig. 3. Lidar RHI scans of the El Portal plume on 28 Jul 2014. (a)–(c) Smoke backscatter. (d),(e) Radial velocity. Times are in PDT.

troposphere (e.g., Butts and Wragg fires) to large fires that burned for months and produced episodic plumes reaching the upper troposphere (e.g., Rim, Rough, Sobranes, and Pioneer fires). Figure 2, which provides pictures of the plumes from a number of fires, shows the range of plumes observed. A subset of fires, including the Bald, Eiler, Rocky, Rim, King, and Pioneer, produced plumes that developed pyroCu/pyroCb (Table 2). Details of the Bald fire pyroCb event are available in Lareau and Clements (2016). PyroCu were also observed at a number of wildfires where the smoke plumes penetrated only into the midtroposphere (e.g., Rough and Bully fires).

OBSERVATIONS AND RESULTS. In this section, we present selected observations and research findings highlighting aspects of plume behavior observed. These analyses are not intended to be fully developed scientific treatments but, rather, illustrative examples of seldom-observed plume processes that have implications for plume rise and fire behavior. There are three associated RaDFIRE papers that provide more detailed analyses of some of these processes (Lareau and Clements 2015, 2016, 2017).

Horizontal axis vortices and finescale mixing processes. Figure 3 shows a sequence of three lidar RHI scans from the El Portal fire on 28 July 2014 during the plume rise (Fig. 1; Table 2). From these data, it is apparent that the lidar was able to observe both the overall plume structure (e.g., height, width, and tilt) and some of the microscale [*O*(100–1,000) m] mixing processes therein, including the presence of vortical entrainment structures. The smoke backscatter data (Figs. 3a–c), for example, reveal the breakdown and broadening of convective elements as they ascend through the plume as well as the folding of smoke-free air into the plume center. These entraining motions are particularly evident in Fig. 3c as alternating regions of high and low backscatter that correspond with alternating patterns of radially inbound and outbound flow (Fig. 3f). Inbound (outbound) indicates flow toward (away from) the lidar, not the plume. The scale of these mixing structures is on the order of 100 m. In a more detailed analysis of the El Portal plume, Lareau and Clements (2017) demonstrated that these smoke and velocity perturbations covary in time so as to systematically dilute the plume with height (e.g., smoky air is pushed outward, and clear

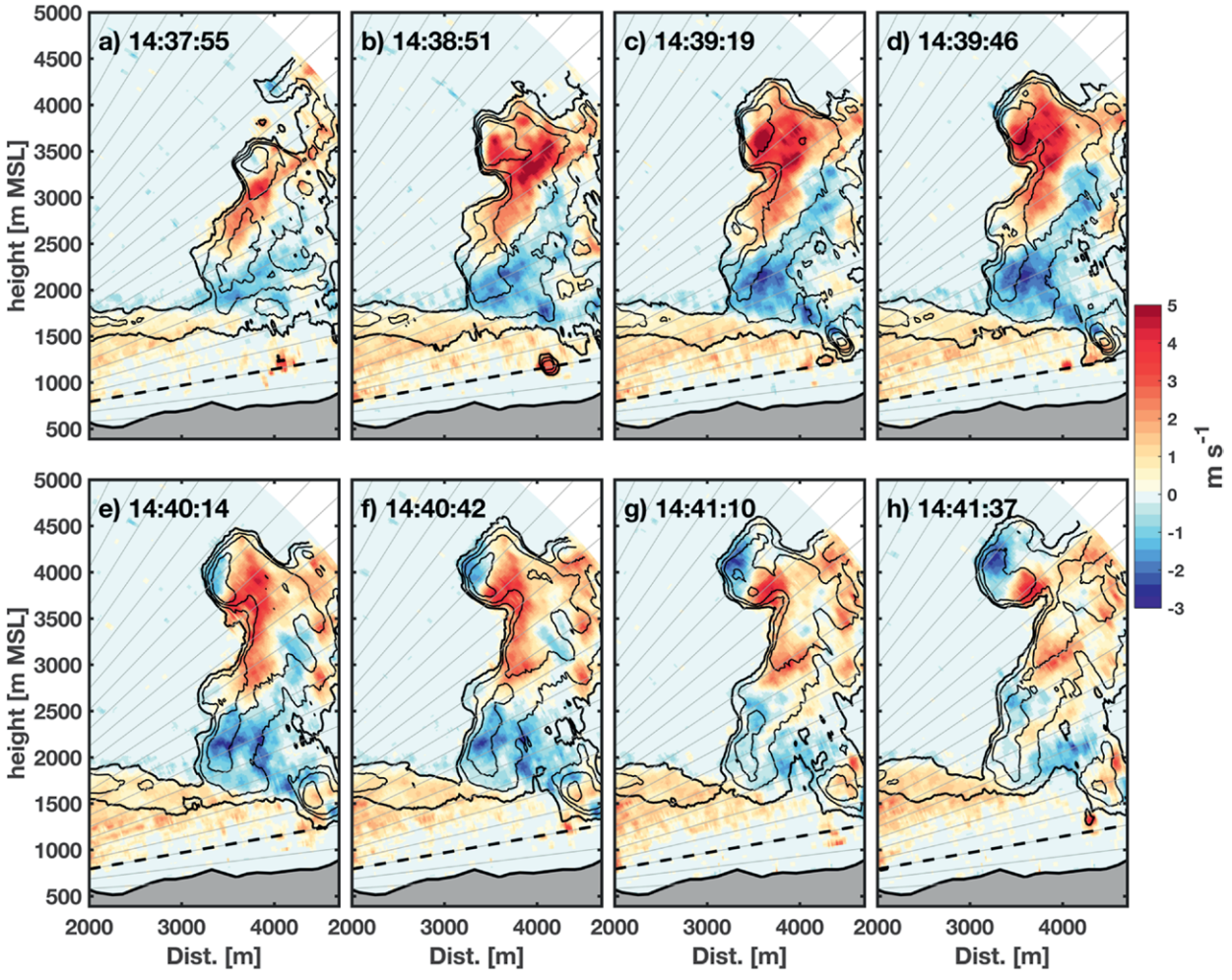

Fig. 4. Lidar RHI scans of the Bully fire plume on 12 Jul 2014 showing the development of a pronounced horizontal axis vortex along the leading plume edge. The smoke backscatter is contoured at −5.8 to −5.0 m^{-1} sr^{-1} in increments of 0.2 m^{-1} sr^{-1} to indicate the plume boundary and smoke concentration. The radial velocity is shaded, with red (blue) indicative of radial velocity away from (toward) the lidar. Lidar radials are shown for reference as light gray lines every 3° in elevation, although the scan resolution is every 0.7°. Times are in PDT.

air is folded inward), thereby giving rise to a Gaussian plume cross section and a linear broadening of the plume with height, consistent with classic plume-rise theory.

Larger kilometer-scale eddies can also contribute to mixing along the plume boundaries. For example, Fig. 4 shows a lidar RHI sequence obtained during the Bully fire on 12 July 2014 (Fig. 1; Table 1). The time sequence shows a deep smoke-filled convective plume extending above the CBL (appearing as the lateral smoke layer) to a height of ~4,500 m above mean sea level (MSL). Along the leading plume edge, a rising convective element, initially devoid of rotation (Figs. 4a–d), developed a pronounced 1-km-wide circulation as it neared the plume top (Figs. 4e–h). The strength of the vorticity ($\Delta V \cong 8$ m s^{-1}; diameter ≅ 800 m) was ~0.02 s^{-1}, which is similar to the horizontal axis vorticity observed in cumulus toroidal circulations (Wang and Geerts 2015). The observed "vortex ring" subsequently flattened and eventually dissipated (not shown).

Similar plume edge vortices were observed on a number of other fires (cf. Fig. 5a in Lareau and Clements 2016). Collectively, these lidar observations have provided the first field-based quantification of the horizontal axis vortex rings described by Church et al. (1980) and McRae and Flannigan (1990).

Whole column rotation. During RaDFIRE, lidar observations detailing the size, strength, and evolution of a long-lived rotating convective column were obtained from the Stoney fire on 20 June 2014 at Fort Hunter Liggett, California (Fig. 1; Table 2). The rotating column formed along a ridge crest and persisted for

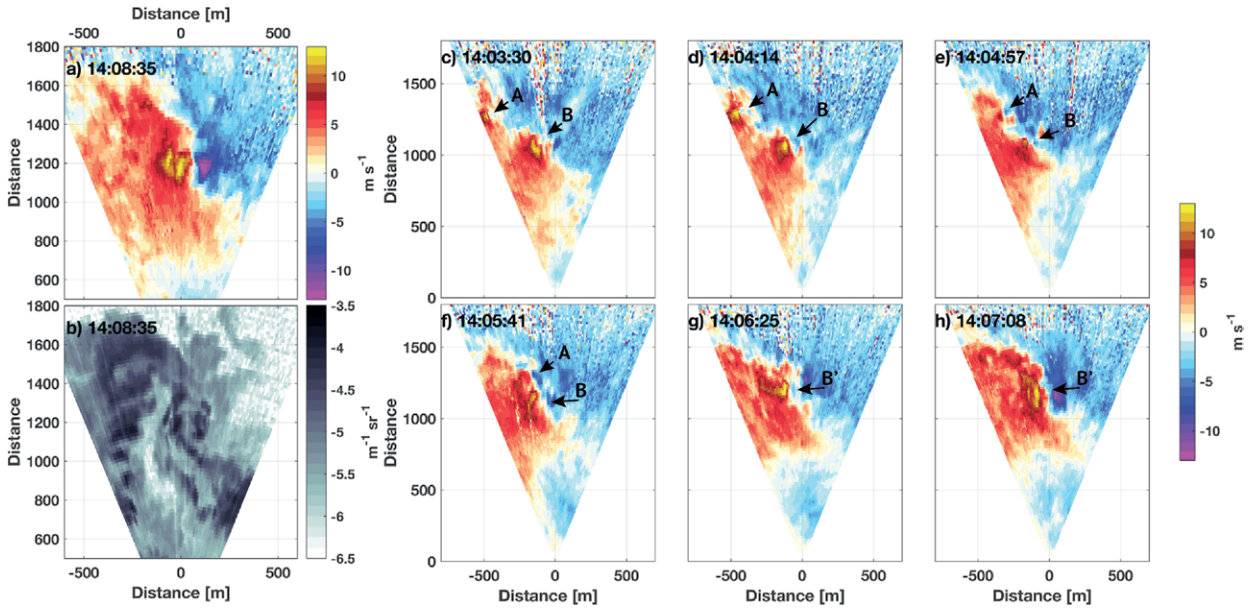

Fig. 5. Lidar PPI scans through the base of a rotating convective column during the Stoney fire on 20 Jun 2014. (a) Radial velocity showing a couplet of inbound (blue) and outbound (red) flow. (b) Corresponding smoke backscatter. (c)–(h) Radial velocity data showing the merger of two smaller vortices. Times are in PDT.

about 30 min, moving only a few hundred meters during that time (see photograph in Fig. 2a). Figure 5 shows the radial velocity and smoke backscatter from a lidar PPI scan slicing through the base of this rotating column during its period of maximum intensity. These data indicate a compact (~150-m diameter) couplet of inbound (–16.2 m s^{-1}; blue shading) and outbound (13.8 m s^{-1}; red shading) radial velocity (Fig. 5a). The implied vertical-axis rotation is anticyclonic, and, indeed, the corresponding smoke backscatter data indicate anticyclonic inwardly spiraling bands of smoky and clear air (Fig. 5b).

The magnitude of the vorticity in the rotating column was estimated using $\zeta \approx 2\nabla V/D$ (Brown and Wood 1991; Bluestein et al. 2004), where ∇V is the difference in extrema of the velocity couplet (30 m s^{-1}) and D is the distance between the extrema (~150 m). The resulting vertical vorticity, 0.4 s^{-1}, is similar to that of dust devils and as large as that of some small tornados (Bluestein et al. 2004) and is an order of magnitude larger than the 0.02 s^{-1} estimated in Banta et al. (1992) for a rotating convective column from a prescribed fire. It was also an order of magnitude larger than the horizontal axis vorticity reported above (Fig. 4) for the observed vortex ring.

Interestingly, the vortex detailed in Figs. 5a and 5b resulted from the merger of two smaller antecedent anticyclonic vortices (Figs. 5c–h). Starting at 1403

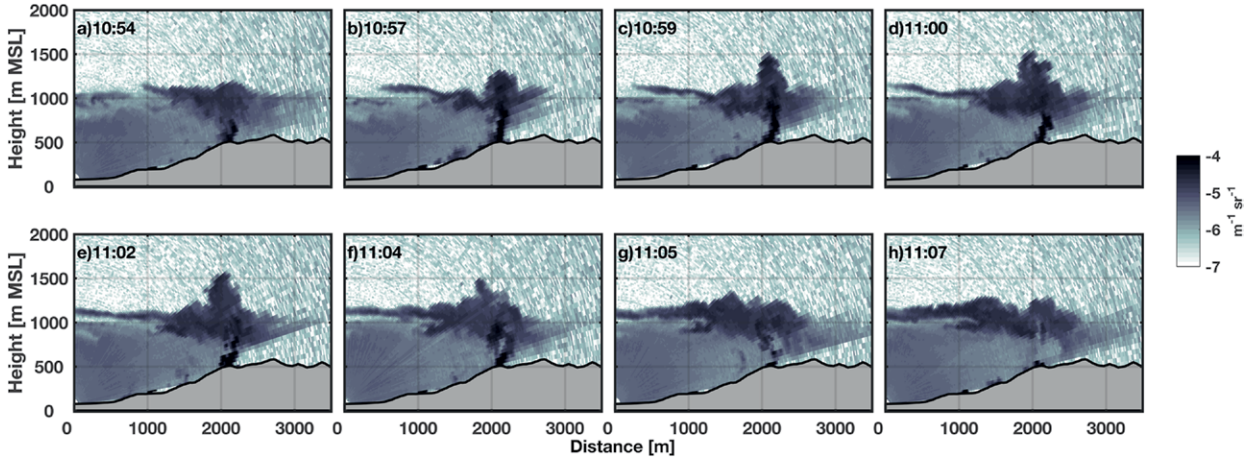

Fig. 6. RHI scans showing the smoke backscatter during a pulse of penetrative convection from the Wragg fire on 23 Jul 2015. Times are in PDT.

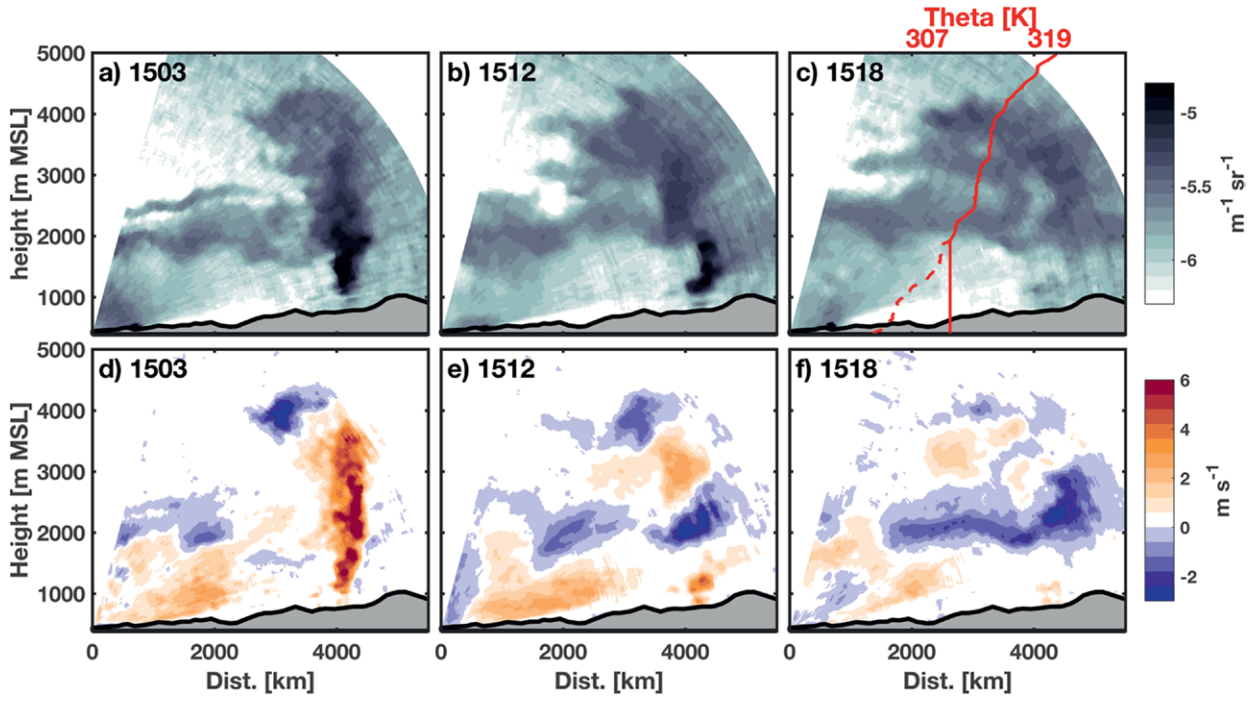

Fig. 7. Sequence of RHI scans showing the dissipation of a plume and subsequent smoke detrainment during the Bully fire on 11 Jul 2014. (a)–(c) Smoke backscatter averaged over four RHI scans ending at the time indicated. In addition, (c) shows the potential temperature profile (red line, top axis) from a radiosonde, including the inferred boundary layer growth (dashed vs solid lines). (d)–(f) Lidar radial velocity data averaged over four RHI scans ending at the time indicated. Times are in PDT.

Pacific daylight time (PDT), the lidar data indicated two distinct velocity couplets (labeled A and B in Figs. 5c–h). The leftmost vortex ("A") approached the other ("B"), which is relatively stationary, over the ensuing two minutes. By 1406 PDT, the vortices had merged to form a single larger and stronger whirl (labeled B′ in Fig. 5). Inspection of a longer series of these scans revealed additional small-scale vortex interactions, and observations revealed helical updrafts (i.e., intertwined vortices). This was consistent with the schematic presented by Church et al. (1980, cf. their Fig. 13).

Penetrative convection and smoke detrainment. Penetrative convection occurs when convective plumes, in this case from wildfires, impinge on stratified layers in the atmosphere (Weil 1988). The degree of plume penetration into the thermally stratified layer (or layers) aloft significantly influences the evolution and transport of smoke (Kahn et al. 2008; Penner et al. 1992; Fromm et al. 2010). While the basic aspects of penetrative convection are understood, the quantification of injection heights and multilayered detrainment processes for wildfires is typically unavailable.

Penetrative convection and smoke detrainment processes were observed during the Wragg fire on 23 July 2015 (Fig. 6) and the Bully fire on 22 July 2014 (Fig. 7). These lidar observations highlighted some of the intricacies of smoke injection above the CBL. The Wragg fire observations showed, for example, a narrow convective plume impinging on, then penetrating through, the capping inversion (Figs. 6a–d). After the initial penetration, the plume dissipated rapidly, and smoke detrained in a single layer slightly above the CBL. In contrast, the multilayered smoke detrainment associated with a deeper penetrative convection was observed during the Bully fire (Fig. 7). In this case, lidar observations detailed the transition of an initially upright convective plume (Figs. 7a,d) into a dissipating plume with discrete smoke detrainment layers aloft (Figs. 7c,f). Using a radiosonde launched near the fire (and adjusted for daytime CBL growth), the altitude of the detraining smoke layers was found to correspond closely to the stable layers aloft (Figs. 7c,f).

While the link between smoke layers and stable layers aloft has been previously demonstrated from satellite observations (Kahn et al. 2008), the characteristics of these finescale detrainment features are unlikely to be resolved by spaceborne remote sensors. Thus, there is a need for more detailed observations of plume behavior in order to inform smoke transport

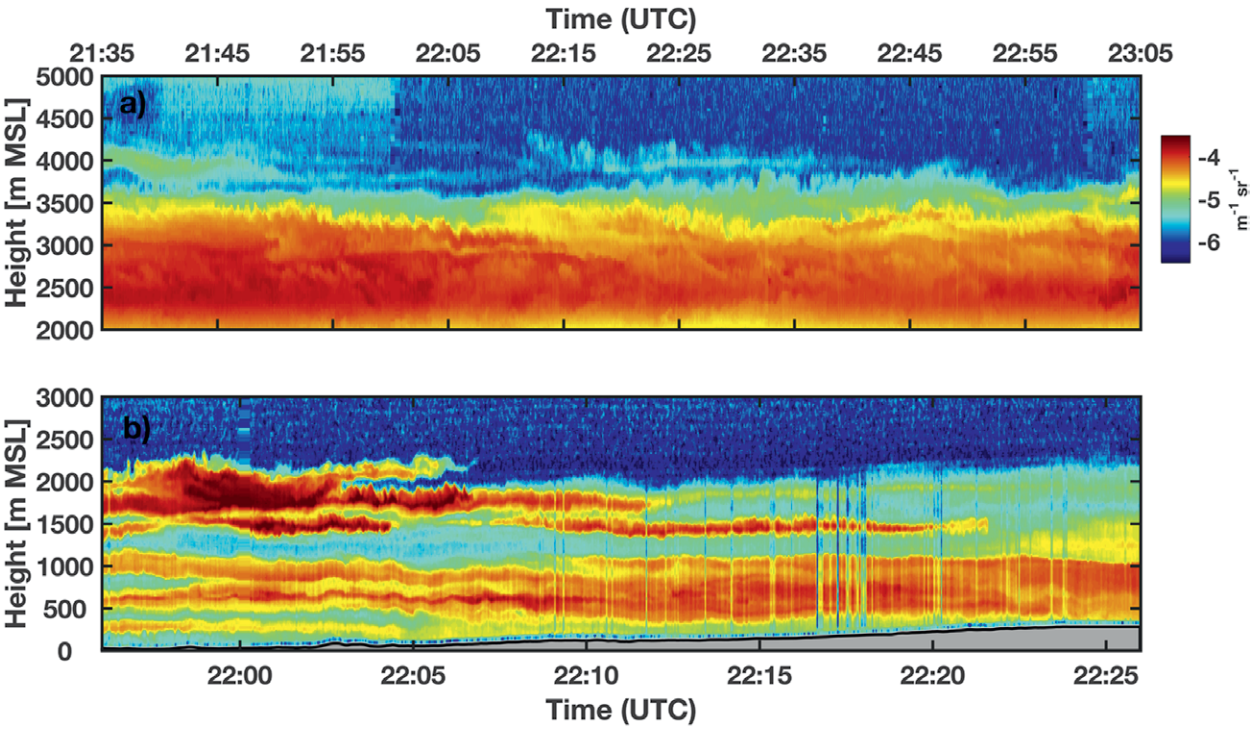

Fig. 8. Lidar backscatter of smoke layers during the (a) Rim fire and (b) Soberanes fire. In (a) the data are collected from fixed-point vertical stare scans, whereas in (b) the data are collected during mobile transects through the fire area. Times are in UTC.

forecasts. This point is reinforced by considering some of the fire-to-fire differences in the smoke detrainment patterns observed during other RaDFIRE deployments. For example, Fig. 8 compares the detrained smoke layers from the Rim fire on 23 August 2013 with those from the Soberanes fire on 27 July 2016. Both sets of observations were collected downwind of the fire source with the vertically pointing lidar. During the Rim fire, the detrained smoke was well mixed and nearly continuous from the surface to 2 km AGL, whereas the detrained smoke from the Soberanes fire occurred in multiple complex layers. Many differences might account for these variations in smoke patterns. These include the structure of the planetary boundary layer, the strength of the plume updrafts, the range of elevations over which the fire is burning, and the presence of vertical wind shear. These complexities must be considered in order to adequately predict smoke dispersion.

Smoke-modified boundary layers. It is known that wildfire smoke can suppress CBL development and even contribute to persistent inversions by reducing the insolation at the surface, a process referred to as *smoke shading* (Robock 1988, 1991; Pahlow et al. 2005). It has also been hypothesized that smoke shading might therefore induce mesoscale circulations because of differential boundary layer development between smoke-filled and smoke-free regions (Segal and Arritt 1992).

To examine smoke shading during RaDFIRE, mobile Doppler lidar transects were conducted to probe the spatial variability of the smoke-filled CBL (see Table 2 for a list of these fires). The most striking examples of smoke shading effects were observed during the Bald and Eiler fires (Fig. 1; Table 2), where the team unexpectedly encountered multiple smoke-induced density currents [detailed analysis available in Lareau and Clements (2015)]. As described in that study, the mobile instruments were used to intersect the leading edge of a propagating near-surface smoke layer as it spread ~25 km across the landscape in a direction counter to that of the ambient wind. Figure 9 shows one such intercept demonstrating many of the canonical features of a density (or gravity) current including an organized updraft in the head region, interfacial wave mixing, and shallower following

Table 3. UWKA flights of RaDFIRE.

No.	Start	End
1	2223 UTC 29 Aug	0142 UTC 30 Aug
2	1631 UTC 30 Aug	1956 UTC 30 Aug
3	2141 UTC 30 Aug	0105 UTC 31 Aug

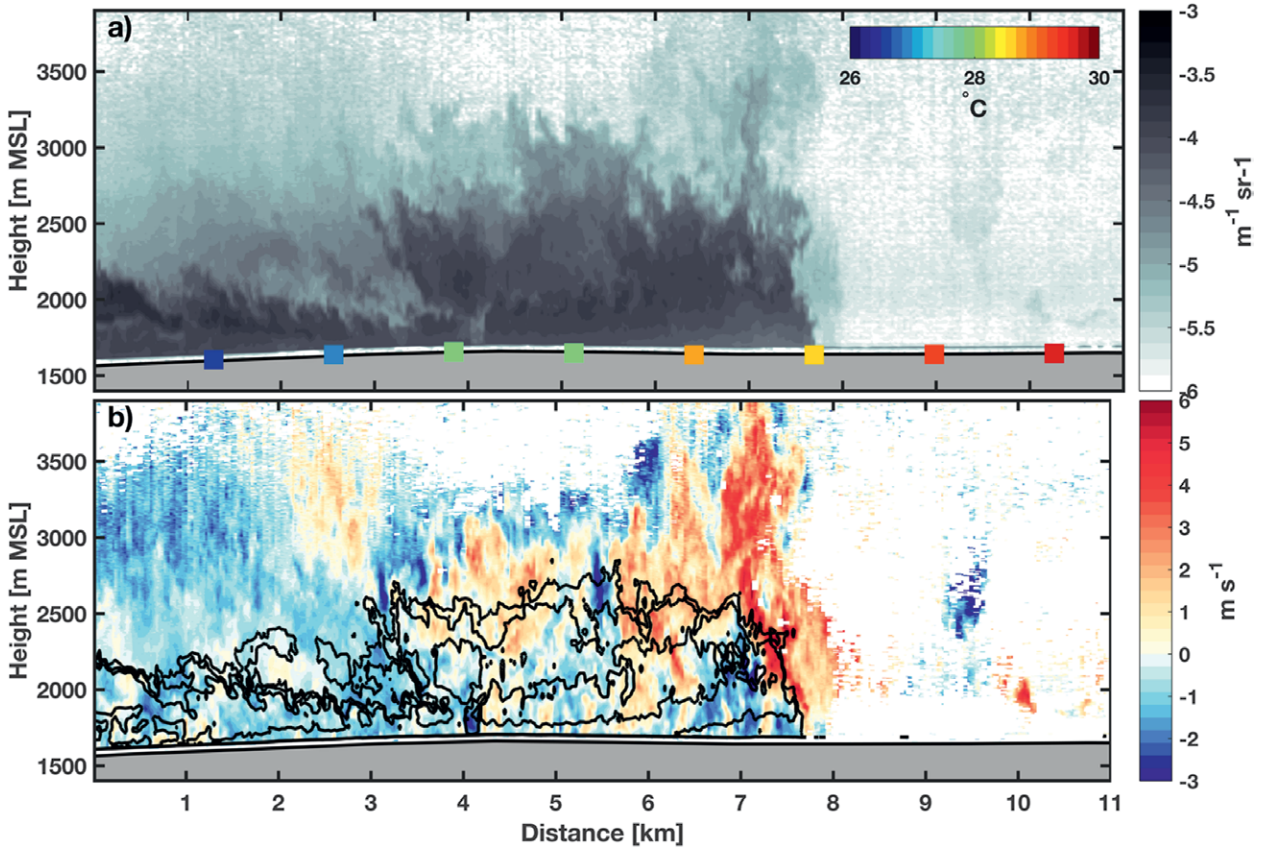

Fig. 9. Mobile lidar intercept of a smoke-filled density current adjacent to the Bald fire on 3 Aug 2014. (a) Smoke backscatter and surface temperature (colored squares). (b) Vertical velocity showing updrafts (red) and downdrafts (blue). The black contours are the attenuated smoke backscatter (levels: −4.5, −4.25, −4 m^{-1} sr^{-1}) and correspond to the backscatter shown in (a). Adapted from Lareau and Clements (2015).

flow (Simpson 1997). In addition, the truck-mounted temperature sensor indicated that the smoke-filled layer was much colder (~3°C) than the ambient air because of the diminished insolation (colored squares in Fig. 9a). A key implication of this previously undocumented process is that a smoke-filled layer was able to propagate against the mean wind, thus constituting an unexpected smoke dispersion pattern unlikely to be predicted by current operational smoke forecasting models (i.e., most operational models do not explicitly include radiative aspects of smoke layers). This limitation has implications for air quality managers who determine smoke impacts on communities downwind of wildfires. If the forecasting tools cannot account for smoke transport resulting from smoke-induced density currents, there is then the potential for unforeseen adverse health effects on these communities.

EXPLORATORY AIRCRAFT OBSERVATIONS. The results from the CSU-MAPS component of RaDFIRE demonstrate the dynamic complexity of wildfire plumes and the feasibility of obtaining observations in the wildfire environment. However, a potential limitation of this approach is that only one observation from the ground was available at any one time, precluding a more complete sampling of the three-dimensional flow field around the fire. To partly overcome this limitation and to facilitate a better kinematic understanding of fire-induced winds in large, active wildfires, the UWKA was used to augment RaDFIRE's sampling strategy.

The RaDFIRE airborne campaign focused on sampling the Pioneer fire, a large wildfire northeast of Boise, Idaho. The fire started on 18 July 2016 and grew to just less than 110,000 acres by the end of 28 August. Over the next three days, the Pioneer fire grew rapidly toward the north, expanding to an area of about 170,000 acres (~688 km^2). The UWKA sampled the fire during three flights on 29–30 August (Table 3): one flight on 29 August and two additional flights on 30 August. The flights focused on a domain in which the fire was actively growing between 28 August and 1 September (Fig. 10). This domain, which includes the Boise National Forest, is characterized by terrain

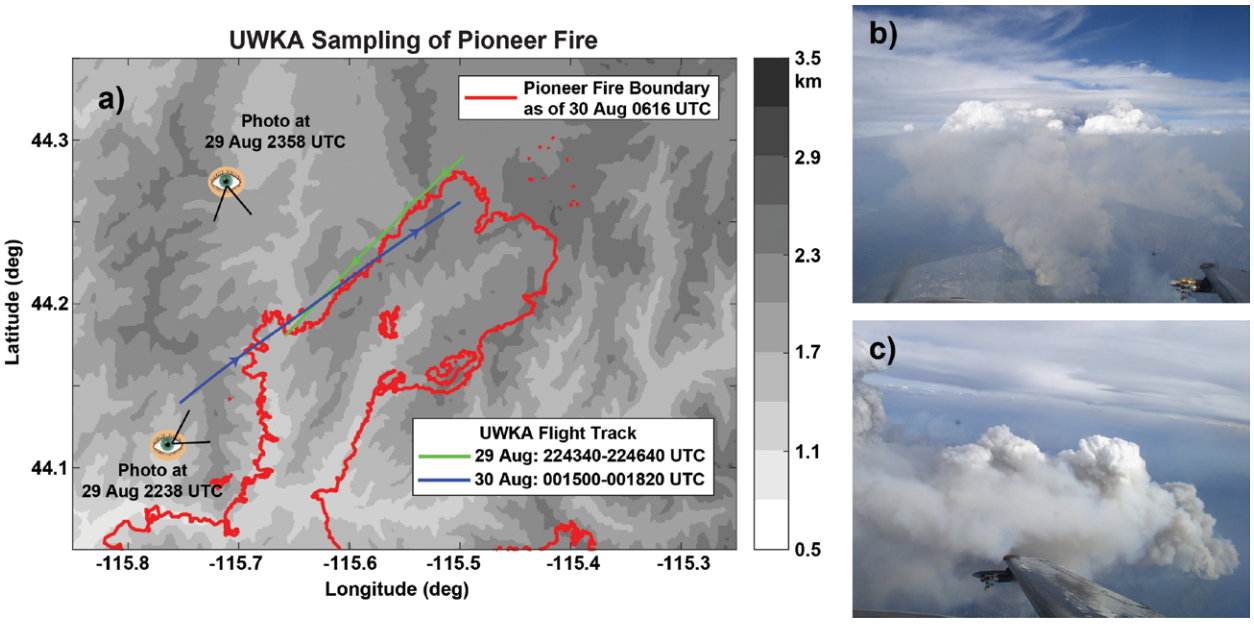

Fig. 10. (a) Topographic map of domain where the UWKA sampled the Pioneer fire. Grayscale for topography shown at right. Boundary of the Pioneer fire as of 0616 UTC 30 Aug is indicated by the red line. Green and blue lines represent the location of UWKA flight legs between 2243:40 and 2246:40 UTC 29 Aug and between 0015:00 and 0018:20 UTC 30 Aug, respectively. The positions and view angles of photographs taken from the UWKA at (b) 2238 and (c) 2358 UTC 29 Aug are indicated.

varying in elevation from ~1 to ~2.5 km MSL (Fig. 10) and vegetation dominated by coniferous trees.

A visual perspective of the Pioneer fire is provided by a photograph taken from the UWKA during the flight on 29 August (Fig. 10b). This photograph was taken at 2238 UTC and is looking toward the northeast. The photograph shows several wildfire smoke plumes ascending from the surface up to an altitude just below the aircraft flight level of ~4.9 km MSL where the background visibility improves dramatically. Above this altitude, the plumes appear to merge into a conglomeration of pyroCu clouds whose tops are well above the aircraft flight level.

In situ observations from a penetration of the pyroCu less than 10 min later (2243:40–2246:40 UTC 29 August) at the same flight level (Fig. 11) depict a very turbulent environment, especially during the first minute of this flight leg tracking from northeast to southwest (Fig. 10). Two relatively narrow updrafts peaking at just below 20 m s^{-1} were followed by a relatively wide updraft peaking at just above 35 m s^{-1} (Fig. 11a). Downdrafts of 2–4 m s^{-1} were evident on both sides of this strong updraft. There was a 3°–4°C air temperature increase from the updraft edges to the updraft peak (Fig. 11b). The relative humidity values within these updrafts were mostly below 60% with relatively small along-track variations compared to later in the leg. Corresponding cloud liquid water contents were only 10–20 mg m^{-3} (Fig. 11a), much smaller than typical cumulus clouds where such values are usually well in excess of 100 mg m^{-3} (e.g., Pruppacher and Klett 1997).

As shown in Fig. 11c, the number concentration of cloud droplets N_{CDP} was also very small (<5 cm^{-3}), while the number concentration of larger particles N_{2DP} was 0.4–0.8 L^{-1}, which is somewhat small for a cumulus cloud, but not unprecedented (e.g., Kingsmill et al. 2004). Further analysis will be required to determine whether these large particles are hydrometeors or ash particles.

A shallower plume was sampled by the WCR during a flight leg spanning 0015:00–0018:20 UTC 30 August and tracking from southwest to northeast (Fig. 10). This plume was on the southwest flank of the earlier-penetrated pyroCu. A photograph taken at 2358 UTC 29 August and looking toward the south-southeast documents its visual character (Fig. 10c). The WCR data shown in Fig. 12 use beams from both the upward- and downward-pointing antennas. Peak reflectivity values of ~−5 dBZ_e were observed near the surface between 0015:50 and 0016:40 UTC (Fig. 12a). These are areas where active fire behavior was evident on the ground. After 0016:40 UTC, the wildfire plume thickened and elevated as it was tilted downwind. Echo tops reached flight level (7.3 km MSL) by ~0017:30 UTC. Reflectivity in the elevated plume was mostly larger than −20 dBZ_e, with several pockets of ~−5 dBZ_e. The Doppler vertical velocities suggested a very turbulent character (Fig. 12b). Updrafts often exceeded 15 m s^{-1} and were

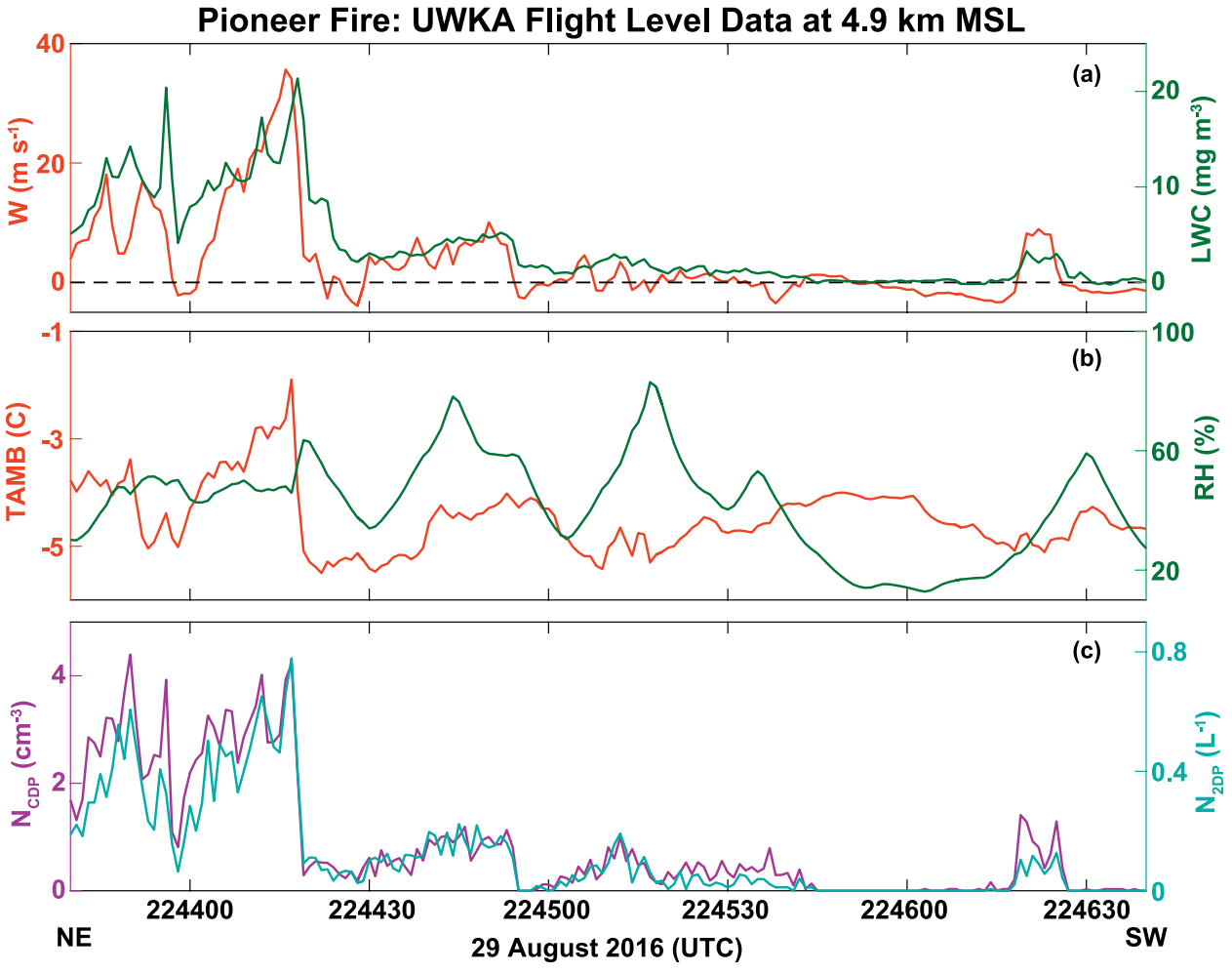

Fig. 11. In situ observations from the UWKA during a flight leg at 4.9 km MSL spanning the period 2243:40–2246:40 UTC 29 Aug and tracking from northeast to southwest (Fig. 2). (a) Vertical air velocity (red) and cloud liquid water content from the Gerber probe (green), (b) air temperature (red) and relative humidity (green), and (c) total cloud droplet concentration from the CDP probe (magenta) and total large-particle concentration from the 2DP probe (cyan).

probably closer to 20 m s^{-1} after accounting for velocity folding (WCR Nyquist velocity is 15.8 m s^{-1}). Relatively weak downdrafts are sometimes evident on the sides of strong updrafts. This is similar to the pattern observed during the pyrocumulus penetration (Fig. 11a).

Collectively, these aircraft observations amount to the first detailed collocated sampling of plume kinematics and microphysical properties, and they may provide insight for future aircraft-based observations of wildfire pyroconvective processes. Additional analyses of these data are now under way to examine, among other topics, how vertical velocity and radar reflectivity vary with height and downwind distance in the observed plumes.

SUMMARY AND FUTURE WORK. The RaDFIRE campaign was a meteorological field experiment aimed at observing and quantifying the plume dynamics and kinematics of active wildfires from within the fire environment. The campaign's deployment strategy required that the research personnel adhere to the National Incident Command protocol for fire line safety and access within the wildfire incident perimeter while making observations. The campaign employed both a rapidly deployable boundary layer profiling system, with Doppler lidar, and an aircraft equipped with a suite of in situ and remote sensors.

Significant advances from RaDFIRE presented here (and detailed in the associated RaDFIRE papers) include the following:

1) Documentation of microscale (100–1,000 m) entrainment structures in wildfire convective plumes, including the quantification of the scale

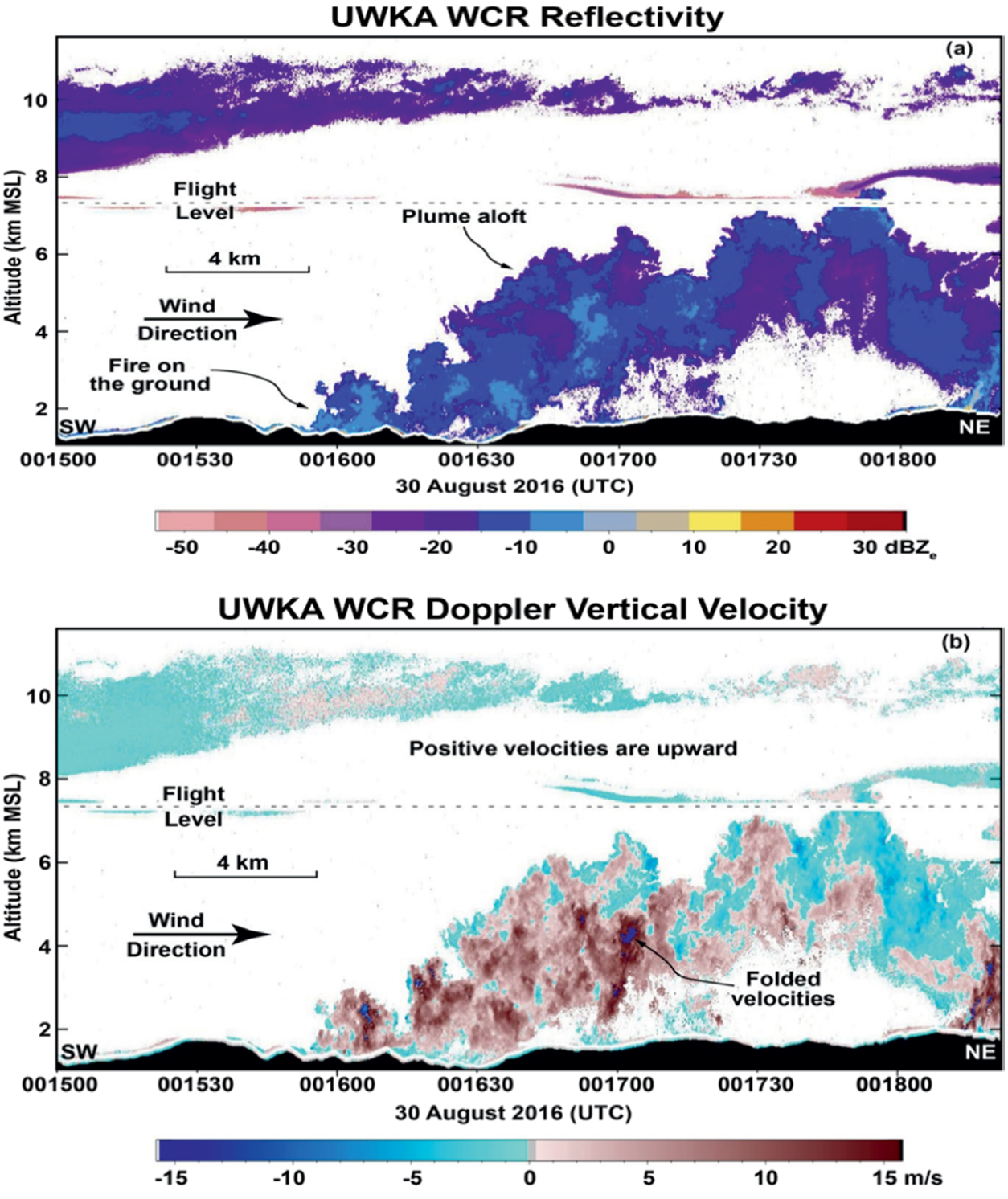

Fig. 12. WCR observations from a UWKA flight leg at 7.3 km MSL spanning 0015:00–0018:20 UTC 30 Aug and tracking from southwest to northeast (Fig. 2). Data from both the upward and downward antennas are combined in this rendering. (a) Reflectivity. (b) Doppler vertical velocity. Color bars at the bottom of both panels indicate values for their corresponding data fields. Positive Doppler vertical velocity values in (b) indicate upward motions. An abrupt change from large positive to large negative Doppler vertical velocities indicates the existence of velocity folding.

and strength of horizontal axis "ring vortices" based on direct observation.
2) Quantification of scale, strength, and evolution of vertical-axis whole-column rotation within a wildfire plume. These observations include details of the merger of two vortices, leading to vortex intensification.
3) Process-level observations of penetrative convective plumes leading to multilayered and complex smoke detrainment. These data show that wildfire plumes exhibit rapid variation in injection height at time scales of $O(10)$ min as they interact with ambient stratification and wind shear.
4) Discovery of previously unknown smoke-induced density currents forming because of reduced insolation beneath smoke layers. This finding has implications for regional-scale smoke transport predictions that are not able to resolve features on this scale arising from smoke radiative effects.
5) In situ measurements obtained by aircraft penetration into the core of a developing pyroCu, highlighting rare documentation of vigorous updrafts aloft exceeding 35 m s^{-1}.
6) Demonstration of the utility of millimeter wave radars in studying the internal structure of wildfire plumes.

In addition to these basic-science findings, another outcome of this project is the development of a dataset for the evaluation of coupled fire–atmosphere and plume-rise models. The RaDFIRE datasets are available online (www.fireweather.org/data-request/). Specifically, data from RaDFIRE provide plume observations during large active wildfires, while previously available datasets were based on small experimental fires only. Additionally, these data will inform the next generation of fire–atmosphere interaction field campaigns because of the demonstrated capabilities and performance of current observational technologies and measurement strategies.

Future campaigns will require a more comprehensive set of observations at multiple scales and from a range of platforms. For example, future deployments should incorporate high-resolution (<10 m) midinfrared (3–5 μm) observations of the fire front. This would facilitate the simultaneous observations of fire behavior characteristics and plume kinematic structures, thereby enabling the linking of plume-scale dynamics to surface fire behavior. Such fire behavior observations were not available during RaDFIRE, so our ability to assess feedbacks (i.e., two-way interactions) between the atmospheric response to the fire and the resulting surface fire behavior was limited.

In conclusion, the observations obtained from RaDFIRE will not only improve our knowledge of the dynamical structures of wildfire plumes but will also advance fire weather science beyond its historical roots of anecdotal descriptions of plume behaviors and use of indices to inform fire weather forecasters and fire behavior analysts. We hope to link these observations with next-generation coupled fire–atmosphere models. This will allow us to provide new tools for fire management to increase firefighter and community safety.

ACKNOWLEDGMENTS. The authors wish to thank the three anonymous reviewers for their comments and suggestions, which improved this manuscript. We thank Jon Contezac and Daisuke Seto for their participation in the early RaDFIRE deployments. We also wish to acknowledge and to thank the Tahoe National Forest for managing the team red card and fire line qualifications. In addition, we appreciate the efforts of the staff at the University of Wyoming King Air Research Aircraft Facility in planning for and executing the RaDFIRE aircraft campaign. This research was funded by the National Science Foundation's Physical and Dynamic Meteorology Program under Awards AGS-1151930 and AGS-1719243.

REFERENCES

Abatzoglou, J. T., and A. P. Williams, 2016: Impact of anthropogenic climate change on wildfire across western US forests. *Proc. Natl. Acad. Sci. USA*, **113**, 11 770–11 775, https://doi.org/10.1073/pnas.1607171113.

Andreae, M. O., D. Rosenfeld, P. Artaxo, A. A. Costa, G. P. Frank, K. M. Longo, and M. A. F. Silva-Dias, 2004: Smoking rain clouds over the Amazon. *Science*, **303**, 1337–1342, https://doi.org/10.1126/science.1092779.

Banta, R. M., L. D. Olivier, E. T. Holloway, R. A. Kropfli, B. W. Bartram, R. E. Cupp, and M. J. Post, 1992: Smoke-column observations from two forest fires using Doppler lidar and Doppler radar. *J. Appl. Meteor.*, **31**, 1328–1349, https://doi.org/10.1175/1520-0450(1992)031<1328:SCOFTF>2.0.CO;2.

Barbero, R., J. T. Abatzoglou, N. K. Larkin, C. A. Kolden, and B. Stocks, 2015: Climate change presents increased potential for very large fires in the contiguous United States. *Int. J. Wildland Fire*, **24**, 892–899, https://doi.org/10.1071/WF15083.

Bluestein, H. B., C. C. Weiss, and A. L. Pazmany, 2004: Doppler radar observations of dust devils in Texas. *Mon. Wea. Rev.*, **132**, 209–224, https://doi

.org/10.1175/1520-0493(2004)132<0209:DROODD>2.0.CO;2.

Brown, R. A., and V. T. Wood, 1991: On the interpretation of single-Doppler velocity patterns within severe thunderstorms. *Wea. Forecasting*, **6**, 32–48, https://doi.org/10.1175/1520-0434(1991)006<0032:OTIOSD>2.0.CO;2.

Browning, K. A., and R. Wexler, 1968: The determination of kinematic properties of a wind field using Doppler radar. *J. Appl. Meteor.*, **7**, 105–113, https://doi.org/10.1175/1520-0450(1968)007<0105:TDOKPO>2.0.CO;2.

Byram, G. M., 1959: Combustion of forest fuels. *Forest Fire: Control and Use*, K. P. Davis, Ed., McGraw-Hill, 61–89.

Church, C. R., J. T. Snow, and J. Dessens, 1980: Intense atmospheric vortices associated with a 1000 MW fire. *Bull. Amer. Meteor. Soc.*, **61**, 682–694, https://doi.org/10.1175/1520-0477(1980)061<0682:IAVAWA>2.0.CO;2.

Clark, T. L., M. A. Jenkins, J. Coen, and D. Packham, 1996: A coupled atmospheric–fire model: Convective feedback on fire line dynamics. *J. Appl. Meteor.*, **35**, 875–901, https://doi.org/10.1175/1520-0450(1996)035<0875:ACAMCF>2.0.CO;2.

Clements, C. B., and A. J. Oliphant, 2014: The California State University Mobile Atmospheric Profiling System: A facility for research and education in boundary layer meteorology. *Bull. Amer. Meteor. Soc.*, **95**, 1713–1724, https://doi.org/10.1175/BAMS-D-13-00179.1.

Coen, J., S. Mahalingam, and J. Daily, 2004: Infrared imagery of crown-fire dynamics during FROSTFIRE. *J. Appl. Meteor.*, **43**, 1241–1259, https://doi.org/10.1175/1520-0450(2004)043<1241:IIOCDD>2.0.CO;2.

Countryman, C. M., 1971: Fire whirls…why, when, and where. USFS Pacific Southwest Research Station Rep., 14 pp., www.frames.gov/documents/behaveplus/publications/Countryman_1971_FireWhirls_ocr.pdf.

Cunningham, P., S. L. Goodrick, M. Y. Hussaini, and R. R. Linn, 2005: Coherent vortical structures in numerical simulations of buoyant plumes from wildland fires. *Int. J. Wildland Fire*, **14**, 61–75, https://doi.org/10.1071/WF04044.

Damoah, R., and Coauthors, 2004: Around the world in 17 days—Hemispheric-scale transport of forest fire smoke from Russia in May 2003. *Atmos. Chem. Phys.*, **4**, 1311–1321, https://doi.org/10.5194/acp-4-1311-2004.

Dennison, P., S. Brewer, J. Arnold, and M. Moritz, 2014: Large wildfire trends in the western United States, 1984–2011. *Geophys. Res. Lett.*, **41**, 2928–2933, https://doi.org/10.1002/2014GL059576.

Flannigan, M. D., M. A. Krawchuk, W. J. de Groot, B. M. Wotton, and L. M. Gowman, 2009: Implications of changing climate for global wildland fire. *Int. J. Wildland Fire*, **18**, 483–507, https://doi.org/10.1071/WF08187.

Forthofer, J. A., and S. L. Goodrick, 2011: Vortices and wildland fire. Synthesis of knowledge of extreme fire behavior: Volume I for fire managers, Pacific Northwest Research Station General Tech. Rep. PNW-GTR-854, 89–105, www.fs.fed.us/pnw/pubs/pnw_gtr854.pdf.

Fromm, M. D., and R. Servranckx, 2003: Transport of forest fire smoke above the tropopause by supercell convection. *Geophys. Res. Lett.*, **30**, 1542, https://doi.org/10.1029/2002GL016820.

——, A. Tupper, D. Rosenfeld, R. Servranckx, and R. McRae, 2006: Violent pyro-convective storm devastates Australia's capital and pollutes the stratosphere. *Geophys. Res. Lett.*, **33**, L05815, https://doi.org/10.1029/2005GL025161.

——, D. T. Lindsey, R. Servranckx, G. Yue, T. Trickl, R. Sica, and S. Godin-Beekmann, 2010: The untold story of pyrocumulonimbus. *Bull. Amer. Meteor. Soc.*, **91**, 1193–1209, https://doi.org/10.1175/2010BAMS3004.1.

Kahn, R. A., Y. Chen, D. L. Nelson, F.-Y. Leung, Q. Li, D. J. Diner, and J. A. Logan, 2008: Wildfire smoke injection heights—Two perspectives from space. *Geophys. Res. Lett.*, **35**, L04809, https://doi.org/10.1029/2007GL032165.

Kingsmill, D. E., and Coauthors, 2004: TRMM common microphysics products: A tool for evaluating spaceborne precipitation retrieval algorithms. *J. Appl. Meteor.*, **43**, 1598–1618, https://doi.org/10.1175/JAM2151.1.

Lang, T. J., and S. A. Rutledge, 2006: Cloud-to-ground lightning downwind of the 2002 Hayman forest fire in Colorado. *Geophys. Res. Lett.*, **33**, L03804, https://doi.org/10.1029/2005GL024608.

——, ——, B. Dolan, P. Krehbiel, W. Rison, and D. T. Lindsey, 2014: Lightning in wildfire smoke plumes observed in Colorado during summer 2012. *Mon. Wea. Rev.*, **142**, 489–507, https://doi.org/10.1175/MWR-D-13-00184.1.

Lareau, N. P., and C. B. Clements, 2015: Cold smoke: Smoke-induced density currents cause unexpected smoke transport near large wildfires. *Atmos. Chem. Phys.*, **15**, 11 513–11 520, https://doi.org/10.5194/acp-15-11513-2015.

——, and ——, 2016: Environmental controls on pyrocumulus and pyrocumulonimbus initiation and

development. *Atmos. Chem. Phys.*, **16**, 4005–4022, https://doi.org/10.5194/acp-16-4005-2016.

——, and ——, 2017: The mean and turbulent properties of a wildfire convective plume. *J. Appl. Meteor. Climatol.*, **56**, 2289–2299, https://doi.org/10.1175/JAMC-D-16-0384.1.

Luderer, G., J. Trentmann, T. Winterrath, C. Textor, M. Herzog, H. F. Graf, and M. O. Andreae, 2006: Modeling of biomass smoke injection into the lower stratosphere by a large forest fire (Part II): Sensitivity studies. *Atmos. Chem. Phys.*, **6**, 5261–5277, https://doi.org/10.5194/acp-6-5261-2006.

——, ——, and M. O. Andreae, 2009: A new look at the role of fire-released moisture on the dynamics of atmospheric pyro-convection. *Int. J. Wildland Fire*, **18**, 554–562, https://doi.org/10.1071/WF07035.

McRae, D. J., and M. D. Flannigan, 1990: Development of large vortices on prescribed fires. *Can. J. For. Res.*, **20**, 1878–1887, https://doi.org/10.1139/x90-252.

Pahlow, M., J. Kleissl, M. B. Parlange, J. M. Ondov, and D. Harrison, 2005: Atmospheric boundary-layer structure observed during a haze event due to forest-fire smoke. *Bound.-Layer Meteor.*, **114**, 53–70, https://doi.org/10.1007/s10546-004-6350-z.

Pearson, G., F. Davies, and C. Collier, 2009: An analysis of the performance of the UFAM pulsed Doppler lidar for observing the boundary layer. *J. Atmos. Oceanic Technol.*, **26**, 240–250, https://doi.org/10.1175/2008JTECHA1128.1.

Penner, J. E., R. E. Dickinson, and C. S. O'Neill, 1992: Effects of aerosol from biomass burning on the global radiation budget. *Science*, **256**, 1432–1434, https://doi.org/10.1126/science.256.5062.1432.

Peterson, D. A., E. J. Hyer, J. R. Campbell, M. D. Fromm, J. W. Hair, C. F. Butler, and M. A. Fenn, 2015: The 2013 Rim fire: Implications for predicting extreme fire spread, pyroconvection, and smoke emissions. *Bull. Amer. Meteor. Soc.*, **96**, 229–247, https://doi.org/10.1175/BAMS-D-14-00060.1.

——, ——, ——, J. E. Solbrig, and M. D. Fromm, 2017: A conceptual model for development of intense pyrocumulonimbus in western North America. *Mon. Wea. Rev.*, **145**, 2235–2255, https://doi.org/10.1175/MWR-D-16-0232.1.

Potter, B. E., 2012: Atmospheric interactions with wildland fire behavior—II. Plume and vortex dynamics. *Int. J. Wildland Fire*, **21**, 802–871, https://doi.org/10.1071/WF11129.

Pruppacher, H. R., and J. D. Klett, 1997: *Microphysics of Clouds and Precipitation*. Kluwer Academic, 954 pp.

Radke, L. F., J. H. Lyons, P. V. Hobbs, D. A. Hegg, D. V. Sandberg, and D. E. Ward, 1990: Airborne monitoring and smoke characterization of prescribed fires on forest lands in western Washington and Oregon. Pacific Northwest Research Station General Tech. Rep. PNW-GTR-251, 81 pp., https://doi.org/10.2737/PNW-GTR-251.

——, and Coauthors, 1991: Particulate and trace gas emissions from large biomass fires in North America. *Global Biomass Burning: Atmospheric, Climatic, and Biospheric Implications*, J. S. Levine, Ed., MIT Press, 209–224.

Reid, J. S., and P. V. Hobbs, 1998: Physical and optical properties of young smoke from individual biomass fires in Brazil. *J. Geophys. Res.*, **103**, 32 013–32 030, https://doi.org/10.1029/98JD00159.

——, R. Koppmann, T. F. Eck, and D. P. Eleuterio, 2005: A review of biomass burning emissions part II: Intensive physical properties of biomass burning particles. *Atmos. Chem. Phys.*, **5**, 799–825, https://doi.org/10.5194/acp-5-799-2005.

Robock, A., 1988: Enhancement of surface cooling due to forest fire smoke. *Science*, **242**, 911–913, https://doi.org/10.1126/science.242.4880.911.

——, 1991: Surface cooling due to forest fire smoke. *J. Geophys. Res.*, **96**, 20 869–20 878, https://doi.org/10.1029/91JD02043.

Rosenfeld, D., M. Fromm, J. Trentmann, G. Luderer, M. O. Andreae, and R. Servranckx, 2007: The Chisholm firestorm: Observed microstructure, precipitation and lightning activity of a pyro-cumulonimbus. *Atmos. Chem. Phys.*, **7**, 645–659, https://doi.org/10.5194/acp-7-645-2007.

Rothermel, R. C., 1991: Predicting behavior and size of crown fires in the northern Rocky Mountains. USDA Research Paper RP-438, 46 pp.

Segal, M., and R. W. Arritt, 1992: Nonclassical mesoscale circulations caused by surface sensible heat-flux gradients. *Bull. Amer. Meteor. Soc.*, **73**, 1593–1604, https://doi.org/10.1175/1520-0477(1992)073<1593:NMCCBS>2.0.CO;2.

Seto, D., and C. B. Clements, 2011: Fire whirl evolution observed during a valley wind-sea breeze reversal. *J. Combust.*, **2011**, 569475, https://doi.org/10.1155/2011/569475.

Simpson, J. E., 1997: *Gravity Currents: In the Environment and the Laboratory*. Cambridge University Press, 244 pp.

Trentmann, J., and Coauthors, 2006: Modeling of biomass smoke injection into the lower stratosphere by a large forest fire (Part I): Reference simulation. *Atmos. Chem. Phys.*, **6**, 5247–5260, https://doi.org/10.5194/acp-6-5247-2006.

Umscheid, M. E., J. P. Monteverdi, and J. M. Davies, 2006: Photographs and analysis of an unusually large

and long-lived firewhirl. *Electron. J. Severe Storms Meteor.*, **1** (2), www.ejssm.org/ojs/index.php/ejssm/article/viewArticle/6/11.

Val Martin, M., J. A. Logan, R. A. Kahn, F.-Y. Leung, D. L. Nelson, and D. J. Diner, 2010: Smoke injection heights from fires in North America: Analysis of 5 years of satellite observations. *Atmos. Chem. Phys.*, **10**, 1491–1510, https://doi.org/10.5194/acp-10-1491-2010.

——, R. A. Kahn, J. A. Logan, R. Paugam, M. Wooster, and C. Ichoku, 2012: Space-based observational constraints for 1-D plume rise models. *J. Geophys. Res.*, **117**, D22204, https://doi.org/10.1029/2012JD018370.

Viegas, D. X., 1998: Convective processes in forest fires. *Buoyant Convection in Geophysical Flows*, E. J. Plate et al., Eds., Springer, 401–420.

Wang, Y., and B. Geerts, 2015: Vertical-plane dual-Doppler radar observations of cumulus toroidal circulations. *J. Appl. Meteor. Climatol.*, **54**, 2009–2026, https://doi.org/10.1175/JAMC-D-14-0252.1.

Wang, Z., and Coauthors, 2012: Single aircraft integration of remote sensing and in situ sampling for the study of cloud microphysics and dynamics. *Bull. Amer. Meteor. Soc.*, **93**, 653–668, https://doi.org/10.1175/BAMS-D-11-00044.1.

Weil, J. C., 1988: Plume rise. *Lectures on Air Pollution Modeling*, A. Venkatram, Ed., Amer. Meteor. Soc., 119–166.

Werth, P. A., 2011: Critical fire weather patterns. Synthesis of knowledge of extreme fire behavior: Volume I for fire managers, Pacific Northwest Research Station General Tech. Rep. PNW-GTR-854, 25–48, www.fs.fed.us/pnw/pubs/pnw_gtr854.pdf.

Westerling, A. L., H. G. Hidalgo, D. R. Cayan, and T. W. Swetnam, 2006: Warming and earlier spring increase western U.S. forest wildfire activity. *Science*, **313**, 940–943, https://doi.org/10.1126/science.1128834.

New Benefit for AMS Members!

MENTORING365

Reach Your Full Potential

Developed in partnership with Earth and space science organizations, Mentoring365 provides mentors and mentees with structured relationship-building tools to develop and attain focused career goals.

AMS
American Meteorological Society

www.mentoring365.org

These fire–atmosphere interactions may include the development of convective plumes, fire-induced inflow winds, and smoke-radiative effects (Potter 2012).

Wildfire convective plumes link fire heat and moisture emissions to vertical and horizontal atmospheric circulations (Viegas 1998). Fire-induced circulations have also been associated with surges in fire spread (Coen et al. 2004) and also modulate smoke transport and injection height (Penner et al. 1992; Fromm and Servranckx 2003; Damoah et al. 2004). While the complex dynamics of wildfire plumes have long been identified as an important component of fire–atmosphere interaction (Byram 1959; Countryman 1971; Rothermel 1991), there is a paucity of quantitative field studies of these pyroconvective dynamics.

Vorticity in wildfire convective plumes impacts plume rise, fire propagation, and fire intensity (McRae and Flannigan 1990; Forthofer and Goodrick 2011; Potter 2012). Types of in-plume vorticity include counterrotating vortex pairs, whole column (vertical axis) vorticity, and horizontal axis plume edge vortices. Anecdotal, photographic, and computer-simulated evidence for these vortical structures is widely available (McRae and Flannigan 1990; Cunningham et al. 2005; Umscheid et al. 2006; Seto and Clements 2011), whereas detailed quantified observations are not. Banta et al. (1992), for example, provided direct measurements (with lidar and radar) of counterrotating vortex pairs and whole column rotation, but how these single instance observations compare to the scale and intensity of vortical structures in other fires is not known.

Beyond vortical structures, fires are also known to produce strong updrafts and horizontal inflow. Using infrared video analyses of crown fires, Clark et al. (1996) derived inflow velocities of ~5–15 m s^{-1}, updrafts up to 30 m s^{-1}, and downdrafts of ~10–20 m s^{-1}. Similarly, Coen et al. (2004) estimated updrafts on the order of 20–30 m s^{-1} near the base of one wildfire convective plume. The horizontal and vertical extent of these inflows and updrafts has not, however, been systematically observed across a broad sample of fires. It is not known, for example, how far outward from a wildfire convective plume inflow winds can be expected to extend.

The factors modulating smoke injection height also remain poorly understood and underobserved. Satellite observations provide observational context, indicating that only a small fraction (4%–12%) of smoke plumes inject smoke above the planetary boundary layer (Kahn et al. 2008; Val Martin et al. 2010) and that fire intensity (measured as fire radiative power) modulates the final injection height (Val Martin et al. 2012; Peterson et al. 2015). Yet process-level observations detailing how and under what conditions plume interactions with wind shear and temperature stratification affect plume rise and smoke detrainment are not typically available. Fires may modify the structure of the planetary boundary layer by reducing the insolation beneath detrained smoke layers (Robock 1988, 1991; Penner et al. 1992). Thus, stable layers and mixing heights near fires may differ from those resolved by forecast models and observed by regional radiosonde networks. These observational deficits, coupled with uncertainties in plume-rise models, led Val Martin et al. (2012) to conclude that direct field measurements of fire and smoke plume properties are required to produce the next major advances in plume-rise modeling.

While pyrocumulus (pyroCu) are relatively common, pyrocumulonimbus (pyroCb) have been linked to stratospheric smoke injection (Fromm and Servranckx 2003; Fromm et al. 2006, 2010), highly polluted cloud compositions (Andreae et al. 2004; Rosenfeld et al. 2007), and both in-cloud and positive polarity lightning (Lang and Rutledge 2006; Lang et al. 2014). The sensitivity of pyroCb to variations in aerosol loading, sensible heat flux, and water vapor have been simulated with dynamical models (Trentmann et al. 2006; Luderer et al. 2006, 2009) and the environmental conditions favoring pyroCb development have recently been examined (Peterson et al. 2017). However, observations of the internal structure and dynamics of these plumes are largely unavailable and pyroCu/pyroCb feedbacks on fire propagation are not yet known.

Meteorological observations near wildfires are rare, especially compared to the established observational record for other atmospheric processes (e.g., convective storms). This observational deficit likely stems from the considerable logistical and safety challenges associated with sampling in the near-fire environment (Viegas 1998), and therefore, there is a need for obtaining observations from within the near-fire environment. The goals of this paper are twofold. First, it summarizes the design and execution of the Rapid Deployments to Wildfires Experiment (RaDFIRE) campaign, fire-selection and deployment strategies, observational tools, and integration with fire management. Second, it highlights some of the seldom documented aspects of fire–atmosphere interactions observed during the campaign.

DEPLOYMENT STRATEGY TO WILDFIRE INCIDENTS. To observe wildfire convective plume dynamics and other fire–atmosphere interactions during active wildfires, a rapid-response deployment

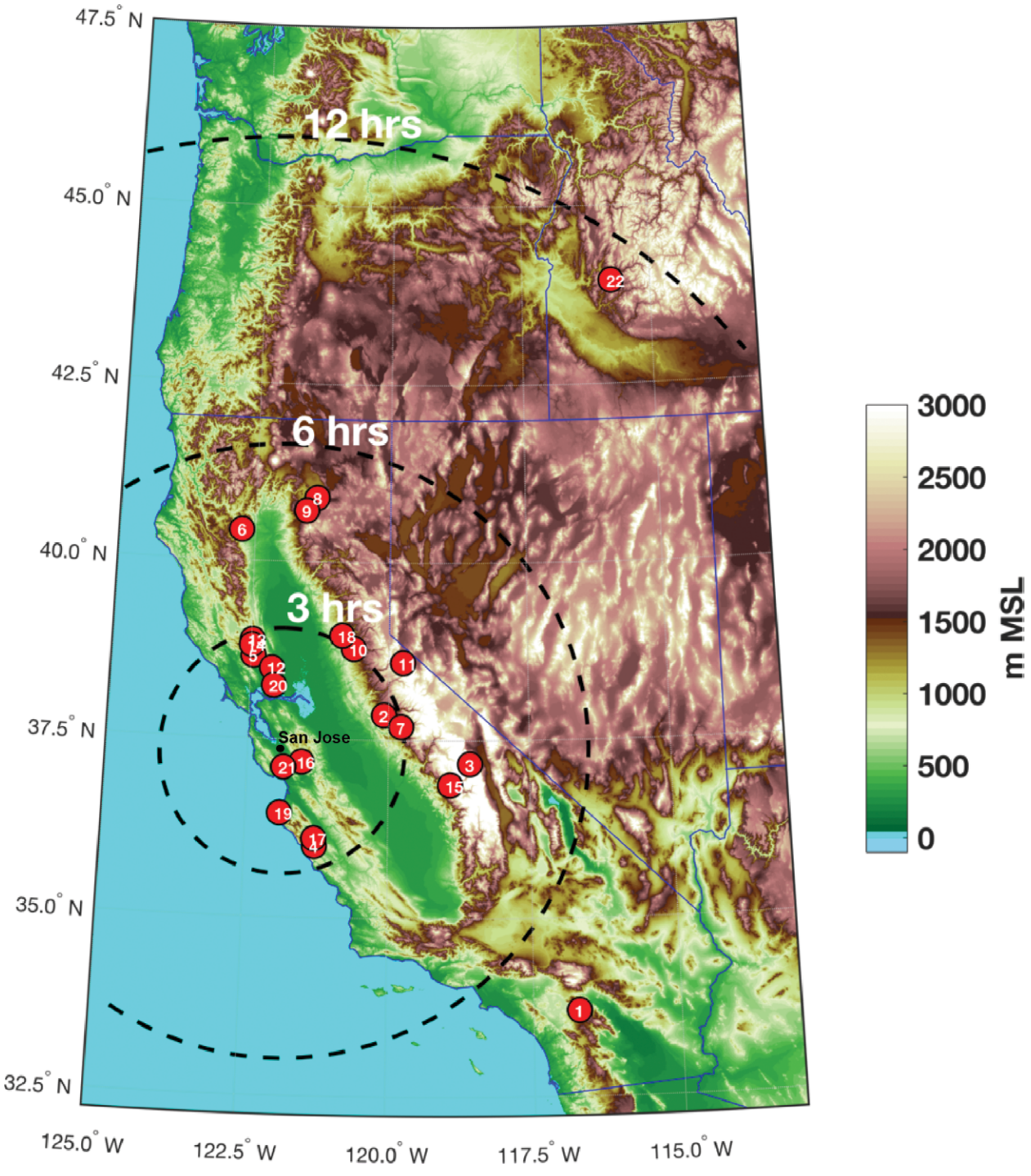

Fig. 1. Map showing RaDFIRE deployments in the western United States. Range rings indicate approximate response times for wildfire incidents from San Jose, CA. Numbers in each circle indicate fire number as listed in Table 1.

strategy was utilized. This strategy required evaluation of individual wildfires for their research potential based on expected spread patterns, weather conditions, and societal impacts. Spread patterns, for example, were estimated from forecast wind and weather patterns, in conjunction with the inspection of the terrain and vegetation for regions conducive to unimpeded fire growth within a deployment window. Deployment decisions were based partly on access considerations, especially the availability of roads and clear lines of sight. Deployments were limited to wildfires within the western United States and within a maximum driving or travel time of 12 h from the RaDFIRE base at San José State University (SJSU) (Fig. 1). All

THE INCIDENT COMMAND SYSTEM

The Incident Command System (ICS) is a standardized system designed to allow emergency responders to adapt management strategies to a variety of incidents with varying levels of complexity. Command of the incident falls to the incident commander (IC) or unified command. Under the incident commander are the command staff (safety, liaison, and information) and four additional functional sections: operations, planning, logistics, and finance and administration. These sections have areas under their purview. The ICS is structured so that only the sections that are needed are staffed and personnel can be added or released as needed.

The operations section is responsible for all operations pertaining to the primary mission of the incident. The planning section is responsible for gathering, assessing, and distributing information related to the incident operations, as well as the preparation of the incident action plan (IAP). It is under the planning section that RaDFIRE generally operates when assigned to an incident, specifically under the guidance of either the incident meteorologist or the fire behavior analyst. Logistics staff address the needs of responders by providing the facilities, services, and equipment needed for an effective response. The finance and administration section is responsible for all cost and administrative needs related to the incident (www.fema.gov/incident-command-system-resources).

When a fire is first detected, the agencies with jurisdiction respond. The first responder on the scene assumes the position of IC until an individual with more training or more appropriate jurisdiction arrives and takes over. The IC directs suppression strategies, provides for responder and public safety, and orders more resources as necessary. A fire may be suppressed or controlled within one operational period, or it may continue into days, weeks, or even months.

As a fire increases in size and/or complexity, the IC divides the fire into functional or area divisions so that he or she can decrease the number of people directly under his or her command. As the fire decreases in complexity, the IC can release resources and combine divisions. In this way, the ICS can be expanded or shrunk according to need.

Different fires may require different objectives. The primary objective across all incidents is to ensure the safety of the public and the responders. Additional objectives might include the protection of property or other valuables at risk, limiting the spread of a fire to a specified area, or allowing the fire to burn a specified area.

deployments were in California with the exception of a single exploratory airborne campaign that used the University of Wyoming King Air (UWKA) to observe plume structures during a large wildfire in Idaho (ID).

Access to wildfire incidents is generally limited to fire-line-qualified personnel (i.e., firefighters and forest managers). This requirement is the foundation of the National Incident Command System (NICS; see sidebar) and limits a research team's proximity to the fire front. To overcome this access constraint, all members of the SJSU research team receive annual fire line training following the standards set by the National Wildfire Coordinating Group. Team members who respond to wildfire incidents are qualified as either "Firefighter Type II" or "Technical Specialists."

SJSU has a formal memorandum of understanding with the Tahoe National Forest to maintain status in the federal Resource Ordering and Status System (ROSS; http://famit.nwcg.gov/applications/ROSS) in order to be requested for a wildfire incident. ROSS "tracks all tactical, logistical, service and support resources mobilized by the incident dispatch community." Generally, the team can be requested in two ways. First, someone at the incident determines that there is a need for the team's observational capability and calls the team to inquire about its availability. Second, when the team determines that an incident is of scientific interest, it may deploy preemptively. In this circumstance, SJSU team members reach out to personnel on the fire and ask to be requested. If a formal request is not granted, the team aborts deployment. When the team is integrated with an incident, members must first go through the incident check-in procedure during which the team is provided logistical information, including maps and the Incident Action Plan. Additionally, the SJSU team radios are synchronized with the incident frequencies. The team will then report to either the NWS incident meteorologist (IMET), the fire behavior analyst (FBAN), or the planning section chief for current fire information and guidance on where to stage the team and the instruments.

There were times that the team deployed to wildfire incidents but was not officially assigned to the incident. In these cases, the team made measurements from a nearby highway, in designated media locations, or at other locations as indicated by fire personnel. These locations, while sometimes not ideal, provided a safe setting for observations.

METHODS AND EXPERIMENTAL DESIGN.

Mobile profiling system. The Fire Weather Research Laboratory operates a rapid-response mobile atmospheric profiling system—the California State University Mobile Atmospheric Profiling System (CSU-MAPS; Clements and Oliphant 2014). It includes a scanning Doppler lidar, microwave profiler, radiosonde system, and automated weather station. The system was designed for boundary layer profiling of the near-fire

environment and to measure smoke plume dynamics. The CSU-MAPS can be operated in either fixed or mobile profiling configurations, enabling rapid response and adaptive measurement strategies. For example, the lidar can be operated while the vehicle is in motion, thereby reducing the startup time if the CSU-MAPS is moved to a different location.

A key component of the CSU-MAPS is the Halo Photonics 1.5-μm scanning Doppler lidar with a range of 9,600 m and a range gate resolution of 18 m (Pearson et al. 2009). The lidar records 1) the attenuated backscatter coefficient and 2) the Doppler velocity. The attenuated backscatter coefficient (hereafter backscatter) is sensitive to micrometer-sized aerosol, including forest fire smoke, which typically exhibits a lognormal particle number distribution with a peak near 0.13 μm and a long tail extending toward coarser particles (Radke et al. 1990, 1991; Banta et al. 1992; Reid and Hobbs 1998; Reid et al. 2005). Banta et al. (1992) showed that infrared lidar backscatter from smoke plumes is primarily from 0.5–2-μm particles, though the contribution from the numerous smaller particles and the sparse larger particles also contributes to the total backscatter. As such, we postprocessed the data as the $\log_{10}$ of the backscatter and interpreted the results as being proportional to the smoke concentrations. In our observations, smoke backscatter typically ranged from -6 to -4 m^{-1} sr^{-1}, and lower values (i.e., -7 m^{-1} sr^{-1}) corresponded to "clear air." The lidar beam sometimes attenuated from heavy aerosol loads in deep plumes and rapidly attenuated with high liquid content of clouds.

The Doppler velocity data were used to investigate aspects of the airflow in and around the convective plumes and within the ambient convective boundary layer (CBL). The velocity data have a precision of ~0.03 m s^{-1} and a range of ±19 m s^{-1}. The velocities reported here, and in other RaDFIRE papers (Lareau and Clements 2015, 2016, 2017), typically result from the motion of airborne smoke and ash particles. Velocity returns are often not available outside of the smoky regions because of the low signal-to-noise ratio (SNR) in pristine mountain environments.

The lidar was operated primarily in a range–height indicator (RHI) scanning mode, with scans centered on the upright portions of the wildfire plumes. Typical RHI sweeps cover ~75° in elevation in ~30 s, providing a beam-to-beam resolution of 41 m at a range of 2 km. Velocity–azimuth display (VAD) scans were also occasionally interspersed with the RHI scans to retrieve the vertical profile of the horizontal

Table 1. Key UWKA instrumentation for RaDFIRE.

Instruments	Characteristics/capabilities
	In situ
Standard flight-level parameters	Navigation (e.g., 3D position, ground speed, airspeed, orientation), winds (e.g., horizontal wind speed and direction, vertical air velocity), state (e.g., pressure, temperature, water vapor)
Droplet Measurement Technologies (DMT) LWC100	Liquid water content for cloud droplets up to ~50 μm
Gerber PVM100	Liquid water content for cloud droplets up to ~60 μm
SkyTech Nevzorov	Total water content and liquid water content
DMT CDP	Size distribution of cloud droplets from 2–50 μm
DMT CIP	Two-dimensional particle imagery with optical-array width of 1.6 mm and resolution of 25 μm; derivation of particle shapes and size distributions
Stratton Park Engineering Company (SPEC) 2DS	Two-dimensional stereographic particle imagery with optical array widths of 1.28 mm and resolutions of 10 mm; derivations of particle shapes and size distributions
Particle Measuring Systems (PMS) 2DP	Two-dimensional particle imagery with optical-array width of 6.4 mm and resolution of 200 μm; derivation of particle shapes and size distributions
	Remote sensing
WCR	95-GHz cloud radar with upward, downward, and down-forward beams; output fields of reflectivity, radial velocity, and spectrum width at spatial resolutions of a few tens of meters
WCL	351-nm cloud lidar with downward beam; output fields of backscatter coefficient and linear depolarization ratio at spatial resolutions of a few meters
Heitronics KT-15.85	Downward-pointing radiative thermometer sensitive to the 9.6–11.5-μm infrared radiation band; estimate of surface temperature
Video camera	Forward and downward visual imagery

Table 2. List of fire deployments.

No.	Incident name	State	Location	Start date	Containment date	Total hectares burned	RADFIRE obs dates	Hectares burned during obs	Obs type	Relevant details
1	Mountain fire	CA	33.705°N, 116.726°W	15 Jul 2013	25 Aug 2013	11,141	20 Jul 2013	0	Lidar, radiosonde, microwave profiler	
2	Rim fire	CA	37.857°N, 120.086°W	17 Aug 2013	24 Oct 2013	104,131	21 Aug 2013 23 Aug 2013 26 Aug 2013 29 Aug 2013 8–9 Sep 2013	15,232 8,094 4,532 2,630 548	Lidar, radiosonde, microwave profiler	PyroCu
3	Shirley fire	CA	35.717°N, 118.555°W	13 Jun 2014	15 Jul 2014	1,030	16–17 Jun 2016	181	Lidar, microwave profiler	
4	Stoney fire	CA	36.006°N, 121.275°W	19 Jun 2014	21 Jun 2014	1,959	20 Jun 2014		Lidar, microwave profiler	Fire whirl
5	Butts fire	CA	38.664°N, 122.454°W	1 Jul 2014	9 Jul 2014	1,740	2 Jul 2014	55	Lidar, radiosonde, microwave profiler	
6	Bully fire	CA	40.431°N, 122.751°W	11 Jul 2014	26 Jul 2014	5,124	11–12 Jul 2014	1,186	Lidar, radiosonde, microwave profiler	
7	El Portal fire	CA	37.691°N, 119.778°W	26 Jul 2014	5 Aug 2014	1,898	28–30 Jul 2016	369	Lidar, radiosonde, microwave profiler	
8	Bald fire	CA	40.901°N, 121.368°W	30 Jul 2014	12 Aug 2014	16,080	2–3 Aug 2016	8,636	Lidar, radiosonde, microwave profiler	PyroCu
9	Eiler fire	CA	40.72°N, 121.562°W	31 Jul 2014	25 Aug 2014	13,118	2–3 Aug 2016	9,996	Lidar, radiosonde, microwave profiler	PyroCu
10	King fire	CA	38.782°N, 120.64°W	13 Sep 2014	9 Oct 2014	39,545	16–17 Sep 2014	13,723	Lidar, radiosonde, microwave profiler	
11	Washington fire	CA	38.592°N, 119.752°W	19 Jun 2015	17 Aug 2015	7,199	23–24 Jun 2015	>40	Lidar, radiosonde, microwave profiler	
12	Wragg fire	CA	38.499°N, 122.115°W	22 Jul 2015	5 Aug 2015	3,258	23 Jul 2015	1,174	Lidar, radiosonde	
13	Rocky fire	CA	38.886°N, 122.476°W	29 Jul 2015	14 Aug 2015	28,100	30 Jul 2015	2,104	Lidar, radiosonde	PyroCu
14	Jerusalem fire	CA	38.814°N, 122.487°W	9 Aug 2015	25 Aug 2015	10,165	13 Aug 2016	202	Lidar	

Table 2. Continued.

No.	Incident name	State	Location	Start date	Containment date	Total hectares burned	RADFIRE obs dates	Hectares burned during obs	Obs type	Relevant details
15	Rough fire	CA	36.874°N, 118.905°W	31 Jul 2015	5 Nov 2015	61,360	18–19 Aug 2015	2,955	Lidar, radiosonde	
16	Henry Coe control burn	CA	37.184°N, 121.534°W	19 Nov 2015	19 Nov 2015	255	19 Nov 2015	255	Lidar, radiosonde	Control burn
17	Coleman fire	CA	36.113°N, 121.289°W	4 Jun 2016	21 Jun 2016	1,020	6–7 Jun 2016	>40	Lidar, radiosonde	
18	Trailhead fire	CA	38.969°N, 120.854°W	28 Jun 2016	18 Jul 2016	2,285	30 Jun 2016	121	Mobile transect, lidar	
19	Soberanes fire	CA	36.461°N, 121.901°W	22 Jul 2016	12 Dec 2016	53,470	26 Jul 2016 11 Aug 2016	2,369 315	Mobile transect, lidar, radiosonde	
20	Cold fire	CA	38.525°N, 122.068°W	2 Aug 2016	12 Aug 2016	2,319	3 Aug 2016	243	Mobile transect, lidar	
21	Loma fire	CA	37.106°N, 121.853°W	26 Sep 2016	12 Dec 2016	1,811	26–28 Sep 2016	1,159	Mobile transect, lidar	
22	Pioneer fire	ID	43.95°N, 115.762°W	18 Jul 2016	4 Nov 2016	76,244	29 Aug 2016 30 Aug 2016	11,807 6,711	Lidar, radar (Wyoming King Air)	PyroCu, PyroCb

wind (Browning and Wexler 1968). Sector plan position indicator (PPI) scans were also conducted on some fires.

In addition to these traditional sampling techniques, mobile lidar observations were also conducted on seven fires. In these scans, the lidar was fixed in vertically staring mode while the truck was in motion, thereby providing time-and-space-resolved measurements of convective boundary layer and smoke layer structures near fires. As we show later, these data provide insights into the fire-modified environment.

UWKA. The UWKA was used as part of an exploratory aircraft campaign within the broader scope of RaDFIRE. The UWKA was equipped with a wide array of in situ and remote sensing instrumentation (Wang et al. 2012). The key instruments deployed on the aircraft during RaDFIRE are outlined in Table 1. The in situ sensors provided information about navigation (aircraft position, speed, and orientation), winds (horizontal and vertical), state parameters (pressure, temperature, and water vapor content), and various cloud physics characteristics (total water content, liquid water content, particle shapes, and size distributions). The primary remote sensing instrument was the W-band (95 GHz) Wyoming Cloud Radar (WCR), which provided reflectivity, radial velocity, and spectrum width along beams directed upward, downward, and down forward. Other remote sensors included the Wyoming Cloud Lidar (WCL) with downward-directed beams that provided backscatter coefficient and linear depolarization ratios, a downward-pointing infrared thermometer, and forward- and downward-pointing video cameras.

The fires. In total, the CSU-MAPS was deployed to 20 wildfires in California (CA) during the RaDFIRE campaign. The UWKA was deployed to one additional fire: the Pioneer fire in Idaho. Fire locations, fire dates, acreage burned, and other details are provided in Table 2 and Fig. 1. Typical deployment durations ranged from 12 h to 3 days.

Collectively, the sampled fires ranged from small short-lived fires producing relatively minor plumes confined to the lower

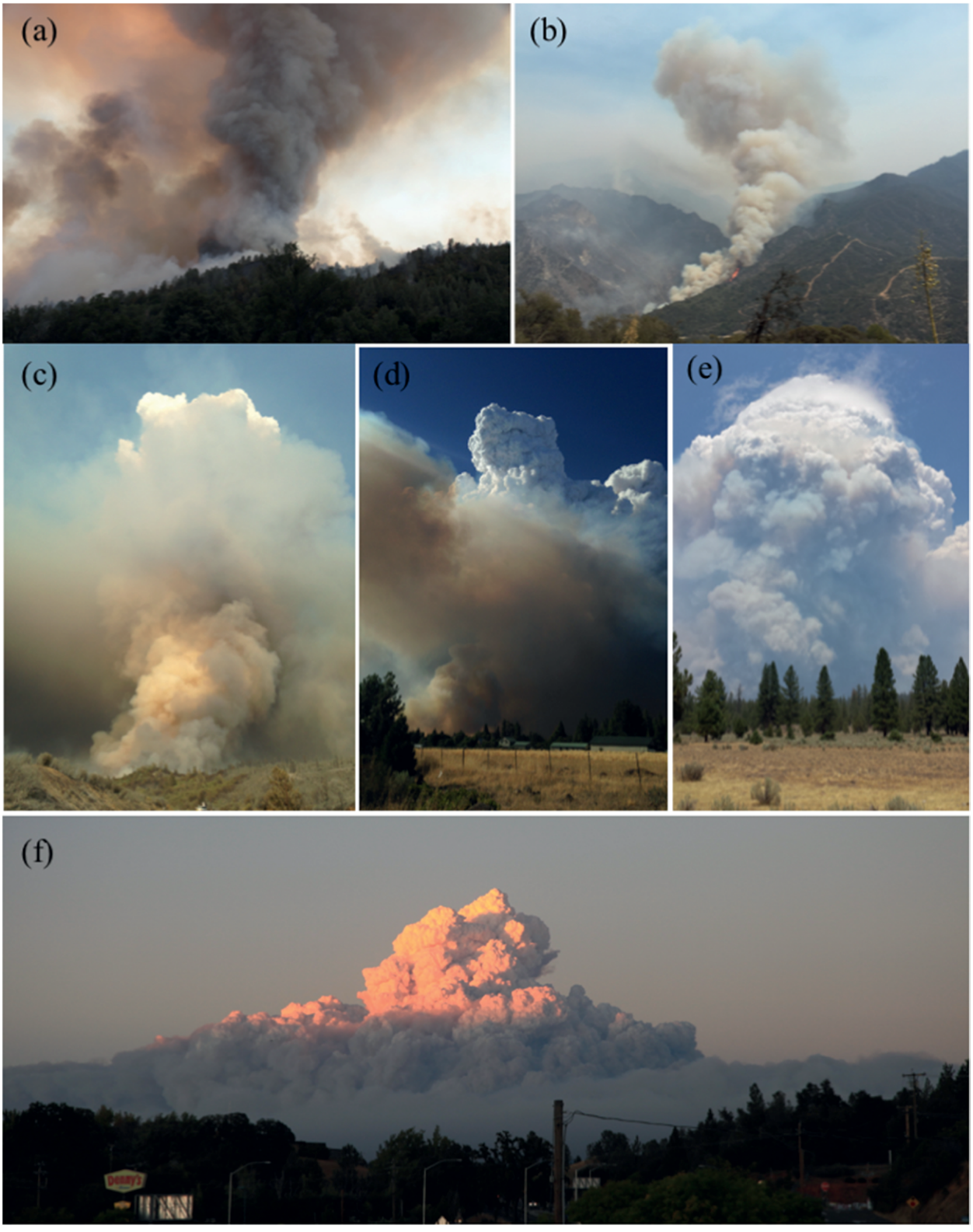

Fig. 2. Photos of wildfire plumes sampled during RaDFIRE. (a) Rotating column of Stoney fire, (b) Rough fire, (c) Rocky fire, (d) Eiler fire, (e) Bald fire, and (f) King fire.

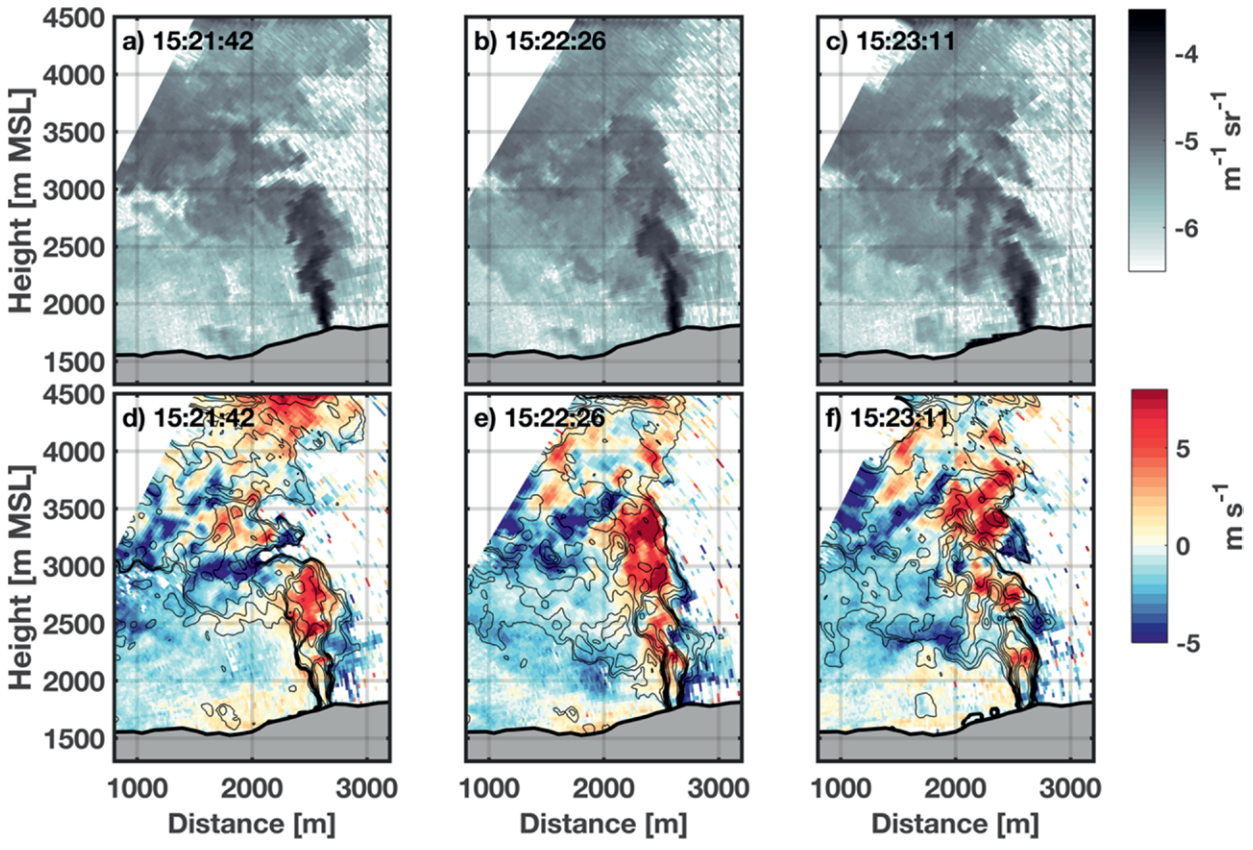

Fig. 3. Lidar RHI scans of the El Portal plume on 28 Jul 2014. (a)–(c) Smoke backscatter. (d),(e) Radial velocity. Times are in PDT.

troposphere (e.g., Butts and Wragg fires) to large fires that burned for months and produced episodic plumes reaching the upper troposphere (e.g., Rim, Rough, Sobranes, and Pioneer fires). Figure 2, which provides pictures of the plumes from a number of fires, shows the range of plumes observed. A subset of fires, including the Bald, Eiler, Rocky, Rim, King, and Pioneer, produced plumes that developed pyroCu/pyroCb (Table 2). Details of the Bald fire pyroCb event are available in Lareau and Clements (2016). PyroCu were also observed at a number of wildfires where the smoke plumes penetrated only into the midtroposphere (e.g., Rough and Bully fires).

OBSERVATIONS AND RESULTS. In this section, we present selected observations and research findings highlighting aspects of plume behavior observed. These analyses are not intended to be fully developed scientific treatments but, rather, illustrative examples of seldom-observed plume processes that have implications for plume rise and fire behavior. There are three associated RaDFIRE papers that provide more detailed analyses of some of these processes (Lareau and Clements 2015, 2016, 2017).

Horizontal axis vortices and finescale mixing processes. Figure 3 shows a sequence of three lidar RHI scans from the El Portal fire on 28 July 2014 during the plume rise (Fig. 1; Table 2). From these data, it is apparent that the lidar was able to observe both the overall plume structure (e.g., height, width, and tilt) and some of the microscale [*O*(100–1,000) m] mixing processes therein, including the presence of vortical entrainment structures. The smoke backscatter data (Figs. 3a–c), for example, reveal the breakdown and broadening of convective elements as they ascend through the plume as well as the folding of smoke-free air into the plume center. These entraining motions are particularly evident in Fig. 3c as alternating regions of high and low backscatter that correspond with alternating patterns of radially inbound and outbound flow (Fig. 3f). Inbound (outbound) indicates flow toward (away from) the lidar, not the plume. The scale of these mixing structures is on the order of 100 m. In a more detailed analysis of the El Portal plume, Lareau and Clements (2017) demonstrated that these smoke and velocity perturbations covary in time so as to systematically dilute the plume with height (e.g., smoky air is pushed outward, and clear

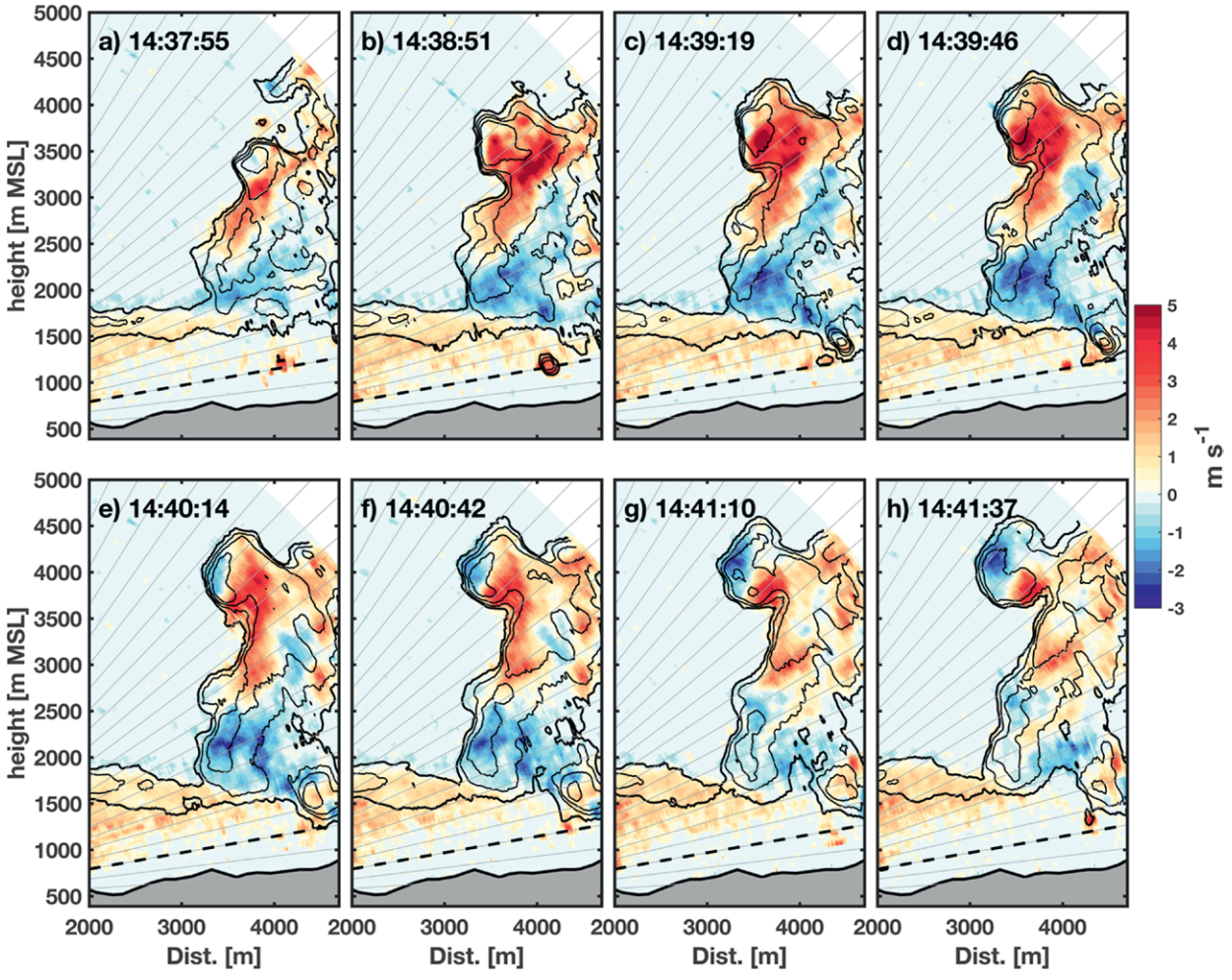

Fig. 4. Lidar RHI scans of the Bully fire plume on 12 Jul 2014 showing the development of a pronounced horizontal axis vortex along the leading plume edge. The smoke backscatter is contoured at −5.8 to −5.0 m^{-1} sr^{-1} in increments of 0.2 m^{-1} sr^{-1} to indicate the plume boundary and smoke concentration. The radial velocity is shaded, with red (blue) indicative of radial velocity away from (toward) the lidar. Lidar radials are shown for reference as light gray lines every 3° in elevation, although the scan resolution is every 0.7°. Times are in PDT.

air is folded inward), thereby giving rise to a Gaussian plume cross section and a linear broadening of the plume with height, consistent with classic plume-rise theory.

Larger kilometer-scale eddies can also contribute to mixing along the plume boundaries. For example, Fig. 4 shows a lidar RHI sequence obtained during the Bully fire on 12 July 2014 (Fig. 1; Table 1). The time sequence shows a deep smoke-filled convective plume extending above the CBL (appearing as the lateral smoke layer) to a height of ~4,500 m above mean sea level (MSL). Along the leading plume edge, a rising convective element, initially devoid of rotation (Figs. 4a–d), developed a pronounced 1-km-wide circulation as it neared the plume top (Figs. 4e–h). The strength of the vorticity ($\Delta V \cong 8$ m s^{-1}; diameter ≅ 800 m) was ~0.02 s^{-1}, which is similar to the horizontal axis vorticity observed in cumulus toroidal circulations (Wang and Geerts 2015). The observed "vortex ring" subsequently flattened and eventually dissipated (not shown).

Similar plume edge vortices were observed on a number of other fires (cf. Fig. 5a in Lareau and Clements 2016). Collectively, these lidar observations have provided the first field-based quantification of the horizontal axis vortex rings described by Church et al. (1980) and McRae and Flannigan (1990).

Whole column rotation. During RaDFIRE, lidar observations detailing the size, strength, and evolution of a long-lived rotating convective column were obtained from the Stoney fire on 20 June 2014 at Fort Hunter Liggett, California (Fig. 1; Table 2). The rotating column formed along a ridge crest and persisted for

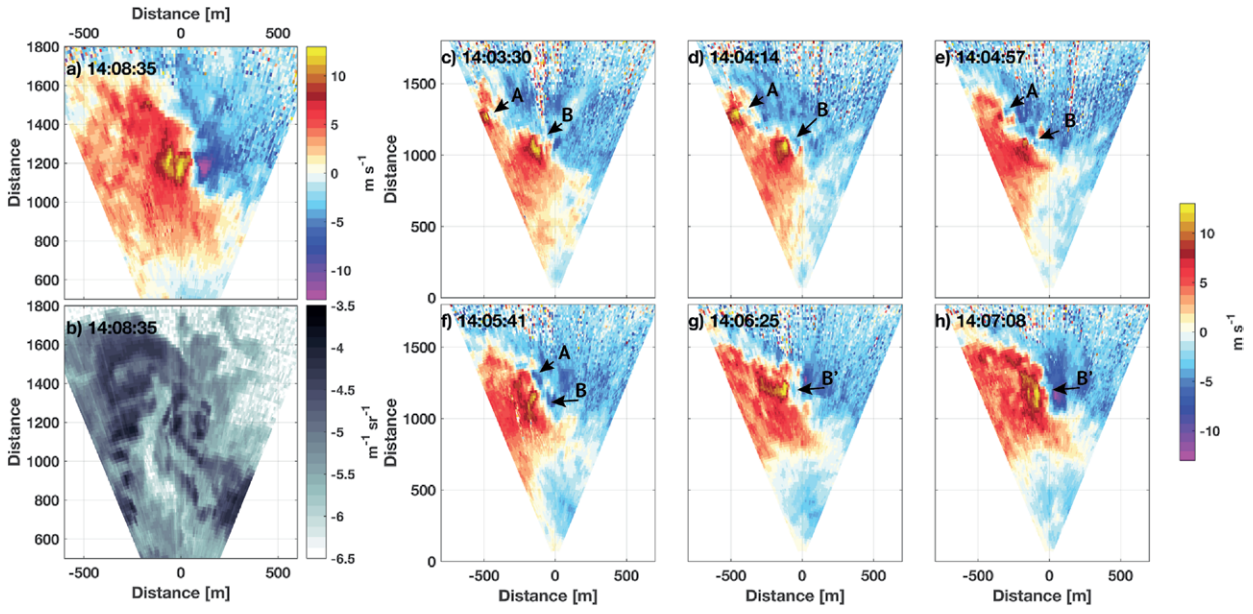

Fig. 5. Lidar PPI scans through the base of a rotating convective column during the Stoney fire on 20 Jun 2014. (a) Radial velocity showing a couplet of inbound (blue) and outbound (red) flow. (b) Corresponding smoke backscatter. (c)–(h) Radial velocity data showing the merger of two smaller vortices. Times are in PDT.

about 30 min, moving only a few hundred meters during that time (see photograph in Fig. 2a). Figure 5 shows the radial velocity and smoke backscatter from a lidar PPI scan slicing through the base of this rotating column during its period of maximum intensity. These data indicate a compact (~150-m diameter) couplet of inbound (–16.2 m s^{-1}; blue shading) and outbound (13.8 m s^{-1}; red shading) radial velocity (Fig. 5a). The implied vertical-axis rotation is anticyclonic, and, indeed, the corresponding smoke backscatter data indicate anticyclonic inwardly spiraling bands of smoky and clear air (Fig. 5b).

The magnitude of the vorticity in the rotating column was estimated using $\zeta \approx 2\nabla V/D$ (Brown and Wood 1991; Bluestein et al. 2004), where ∇V is the difference in extrema of the velocity couplet (30 m s^{-1}) and D is the distance between the extrema (~150 m). The resulting vertical vorticity, 0.4 s^{-1}, is similar to that of dust devils and as large as that of some small tornados (Bluestein et al. 2004) and is an order of magnitude larger than the 0.02 s^{-1} estimated in Banta et al. (1992) for a rotating convective column from a prescribed fire. It was also an order of magnitude larger than the horizontal axis vorticity reported above (Fig. 4) for the observed vortex ring.

Interestingly, the vortex detailed in Figs. 5a and 5b resulted from the merger of two smaller antecedent anticyclonic vortices (Figs. 5c–h). Starting at 1403

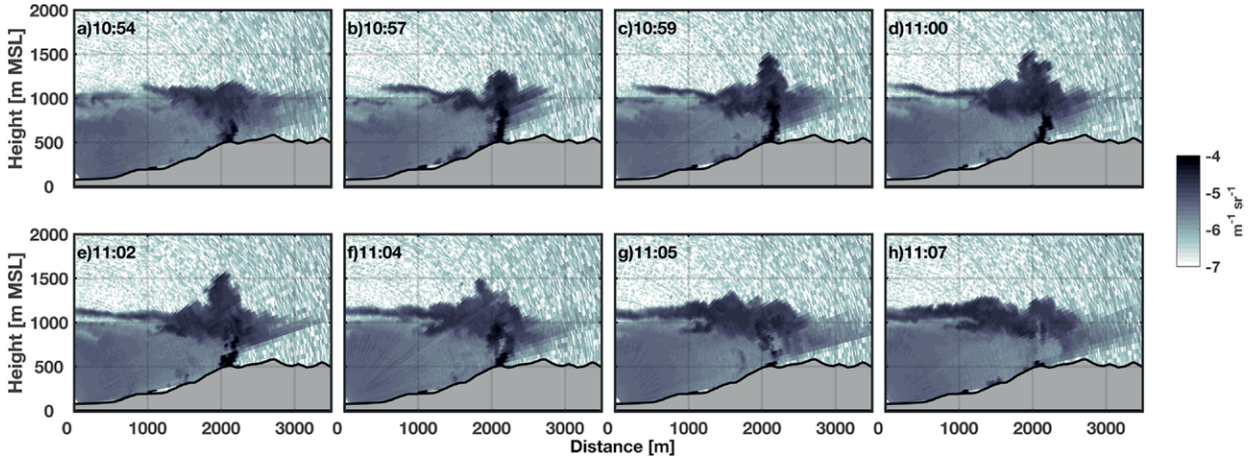

Fig. 6. RHI scans showing the smoke backscatter during a pulse of penetrative convection from the Wragg fire on 23 Jul 2015. Times are in PDT.

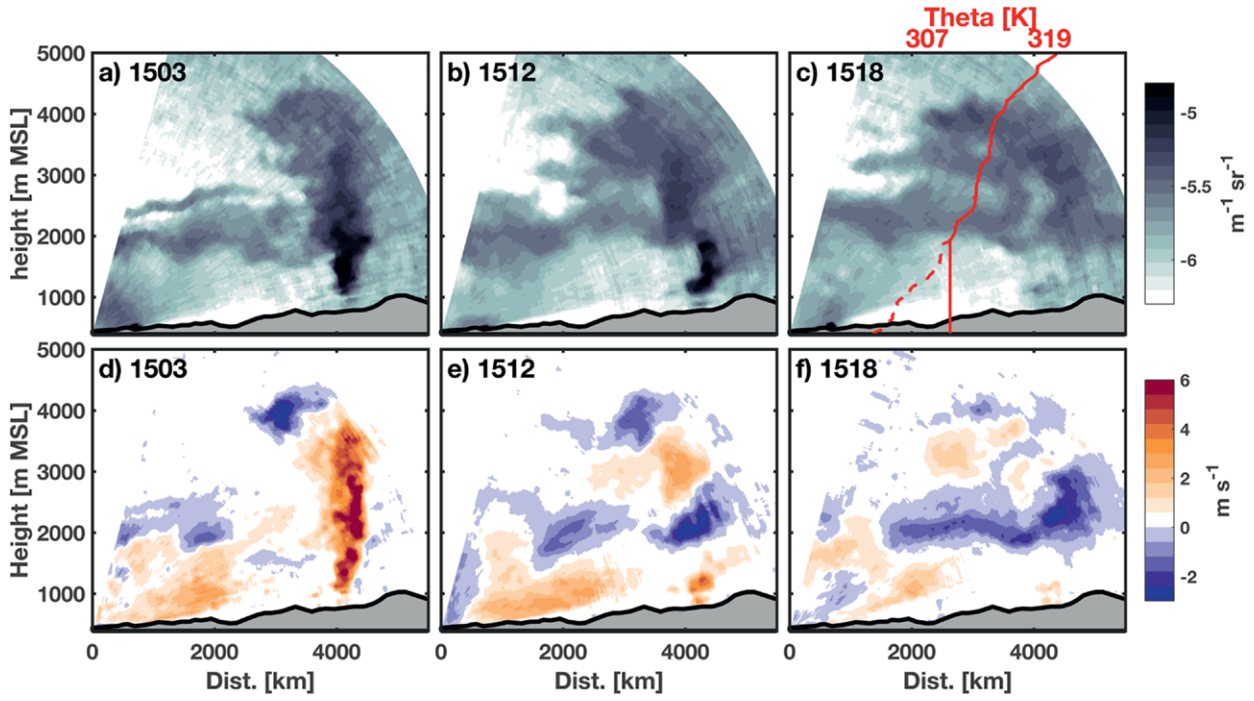

Fig. 7. Sequence of RHI scans showing the dissipation of a plume and subsequent smoke detrainment during the Bully fire on 11 Jul 2014. (a)–(c) Smoke backscatter averaged over four RHI scans ending at the time indicated. In addition, (c) shows the potential temperature profile (red line, top axis) from a radiosonde, including the inferred boundary layer growth (dashed vs solid lines). (d)–(f) Lidar radial velocity data averaged over four RHI scans ending at the time indicated. Times are in PDT.

Pacific daylight time (PDT), the lidar data indicated two distinct velocity couplets (labeled A and B in Figs. 5c–h). The leftmost vortex ("A") approached the other ("B"), which is relatively stationary, over the ensuing two minutes. By 1406 PDT, the vortices had merged to form a single larger and stronger whirl (labeled B′ in Fig. 5). Inspection of a longer series of these scans revealed additional small-scale vortex interactions, and observations revealed helical updrafts (i.e., intertwined vortices). This was consistent with the schematic presented by Church et al. (1980, cf. their Fig. 13).

Penetrative convection and smoke detrainment. Penetrative convection occurs when convective plumes, in this case from wildfires, impinge on stratified layers in the atmosphere (Weil 1988). The degree of plume penetration into the thermally stratified layer (or layers) aloft significantly influences the evolution and transport of smoke (Kahn et al. 2008; Penner et al. 1992; Fromm et al. 2010). While the basic aspects of penetrative convection are understood, the quantification of injection heights and multilayered detrainment processes for wildfires is typically unavailable.

Penetrative convection and smoke detrainment processes were observed during the Wragg fire on 23 July 2015 (Fig. 6) and the Bully fire on 22 July 2014 (Fig. 7). These lidar observations highlighted some of the intricacies of smoke injection above the CBL. The Wragg fire observations showed, for example, a narrow convective plume impinging on, then penetrating through, the capping inversion (Figs. 6a–d). After the initial penetration, the plume dissipated rapidly, and smoke detrained in a single layer slightly above the CBL. In contrast, the multilayered smoke detrainment associated with a deeper penetrative convection was observed during the Bully fire (Fig. 7). In this case, lidar observations detailed the transition of an initially upright convective plume (Figs. 7a,d) into a dissipating plume with discrete smoke detrainment layers aloft (Figs. 7c,f). Using a radiosonde launched near the fire (and adjusted for daytime CBL growth), the altitude of the detraining smoke layers was found to correspond closely to the stable layers aloft (Figs. 7c,f).

While the link between smoke layers and stable layers aloft has been previously demonstrated from satellite observations (Kahn et al. 2008), the characteristics of these finescale detrainment features are unlikely to be resolved by spaceborne remote sensors. Thus, there is a need for more detailed observations of plume behavior in order to inform smoke transport

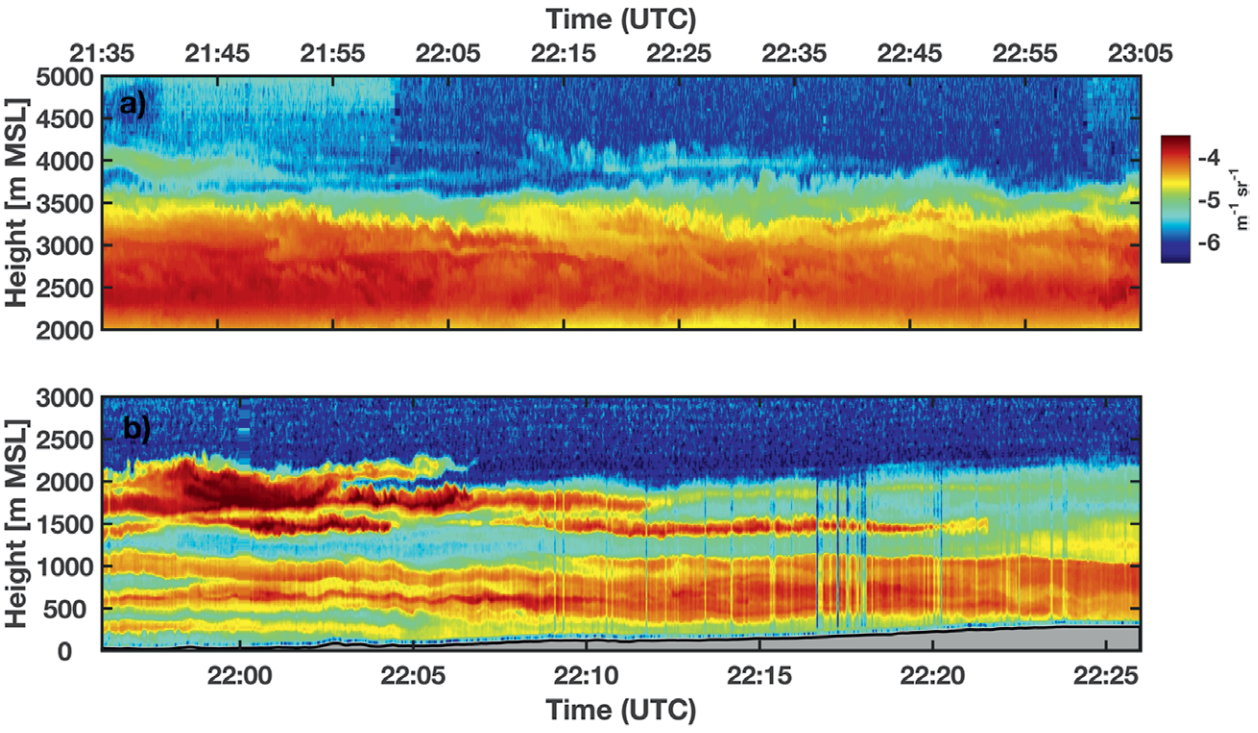

Fig. 8. Lidar backscatter of smoke layers during the (a) Rim fire and (b) Soberanes fire. In (a) the data are collected from fixed-point vertical stare scans, whereas in (b) the data are collected during mobile transects through the fire area. Times are in UTC.

forecasts. This point is reinforced by considering some of the fire-to-fire differences in the smoke detrainment patterns observed during other RaDFIRE deployments. For example, Fig. 8 compares the detrained smoke layers from the Rim fire on 23 August 2013 with those from the Soberanes fire on 27 July 2016. Both sets of observations were collected downwind of the fire source with the vertically pointing lidar. During the Rim fire, the detrained smoke was well mixed and nearly continuous from the surface to 2 km AGL, whereas the detrained smoke from the Soberanes fire occurred in multiple complex layers. Many differences might account for these variations in smoke patterns. These include the structure of the planetary boundary layer, the strength of the plume updrafts, the range of elevations over which the fire is burning, and the presence of vertical wind shear. These complexities must be considered in order to adequately predict smoke dispersion.

Smoke-modified boundary layers. It is known that wildfire smoke can suppress CBL development and even contribute to persistent inversions by reducing the insolation at the surface, a process referred to as *smoke shading* (Robock 1988, 1991; Pahlow et al. 2005). It has also been hypothesized that smoke shading might therefore induce mesoscale circulations because of differential boundary layer development between smoke-filled and smoke-free regions (Segal and Arritt 1992).

To examine smoke shading during RaDFIRE, mobile Doppler lidar transects were conducted to probe the spatial variability of the smoke-filled CBL (see Table 2 for a list of these fires). The most striking examples of smoke shading effects were observed during the Bald and Eiler fires (Fig. 1; Table 2), where the team unexpectedly encountered multiple smoke-induced density currents [detailed analysis available in Lareau and Clements (2015)]. As described in that study, the mobile instruments were used to intersect the leading edge of a propagating near-surface smoke layer as it spread ~25 km across the landscape in a direction counter to that of the ambient wind. Figure 9 shows one such intercept demonstrating many of the canonical features of a density (or gravity) current including an organized updraft in the head region, interfacial wave mixing, and shallower following

Table 3. UWKA flights of RaDFIRE.

No.	Start	End
1	2223 UTC 29 Aug	0142 UTC 30 Aug
2	1631 UTC 30 Aug	1956 UTC 30 Aug
3	2141 UTC 30 Aug	0105 UTC 31 Aug

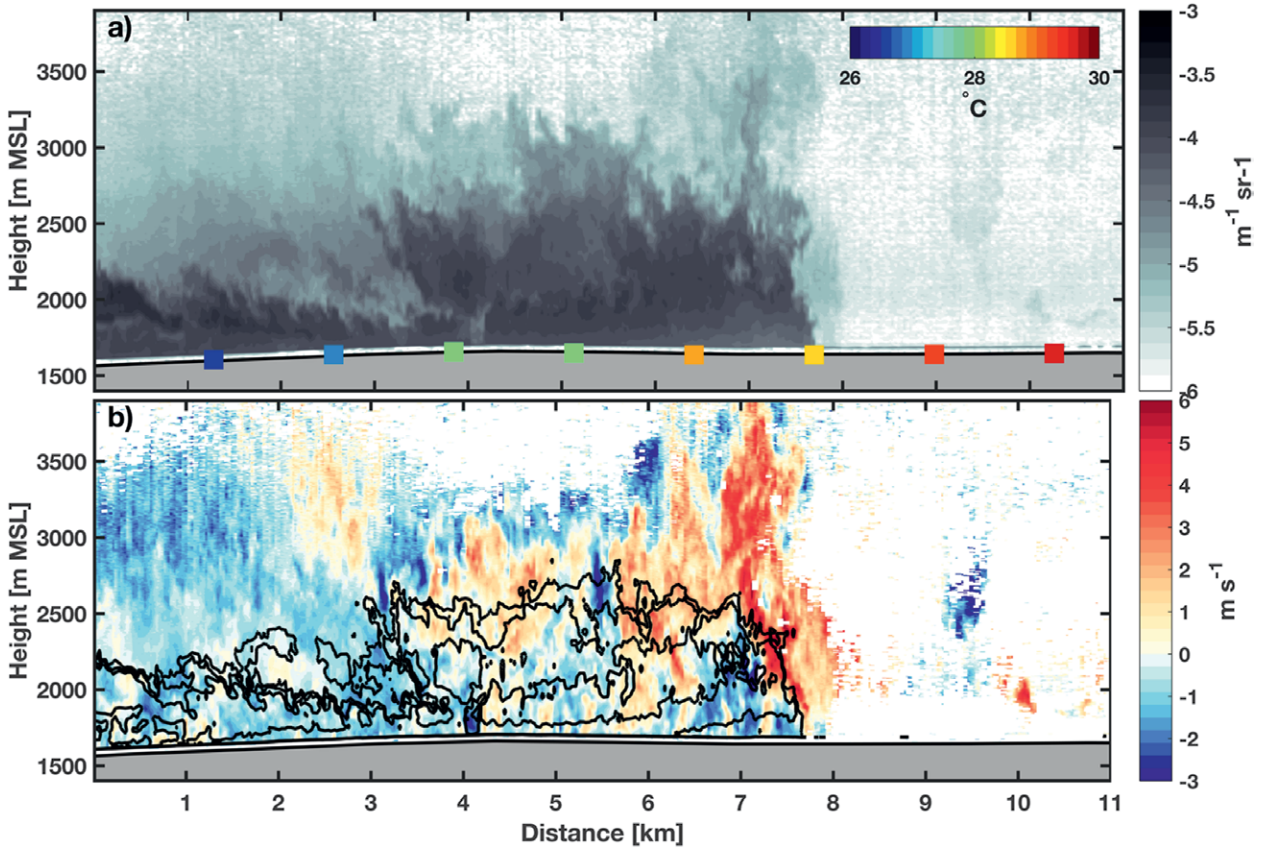

Fig. 9. Mobile lidar intercept of a smoke-filled density current adjacent to the Bald fire on 3 Aug 2014. (a) Smoke backscatter and surface temperature (colored squares). (b) Vertical velocity showing updrafts (red) and downdrafts (blue). The black contours are the attenuated smoke backscatter (levels: −4.5, −4.25, −4 m^{-1} sr^{-1}) and correspond to the backscatter shown in (a). Adapted from Lareau and Clements (2015).

flow (Simpson 1997). In addition, the truck-mounted temperature sensor indicated that the smoke-filled layer was much colder (~3°C) than the ambient air because of the diminished insolation (colored squares in Fig. 9a). A key implication of this previously undocumented process is that a smoke-filled layer was able to propagate against the mean wind, thus constituting an unexpected smoke dispersion pattern unlikely to be predicted by current operational smoke forecasting models (i.e., most operational models do not explicitly include radiative aspects of smoke layers). This limitation has implications for air quality managers who determine smoke impacts on communities downwind of wildfires. If the forecasting tools cannot account for smoke transport resulting from smoke-induced density currents, there is then the potential for unforeseen adverse health effects on these communities.

EXPLORATORY AIRCRAFT OBSERVATIONS. The results from the CSU-MAPS component of RaDFIRE demonstrate the dynamic complexity of wildfire plumes and the feasibility of obtaining observations in the wildfire environment. However, a potential limitation of this approach is that only one observation from the ground was available at any one time, precluding a more complete sampling of the three-dimensional flow field around the fire. To partly overcome this limitation and to facilitate a better kinematic understanding of fire-induced winds in large, active wildfires, the UWKA was used to augment RaDFIRE's sampling strategy.

The RaDFIRE airborne campaign focused on sampling the Pioneer fire, a large wildfire northeast of Boise, Idaho. The fire started on 18 July 2016 and grew to just less than 110,000 acres by the end of 28 August. Over the next three days, the Pioneer fire grew rapidly toward the north, expanding to an area of about 170,000 acres (~688 km^2). The UWKA sampled the fire during three flights on 29–30 August (Table 3): one flight on 29 August and two additional flights on 30 August. The flights focused on a domain in which the fire was actively growing between 28 August and 1 September (Fig. 10). This domain, which includes the Boise National Forest, is characterized by terrain

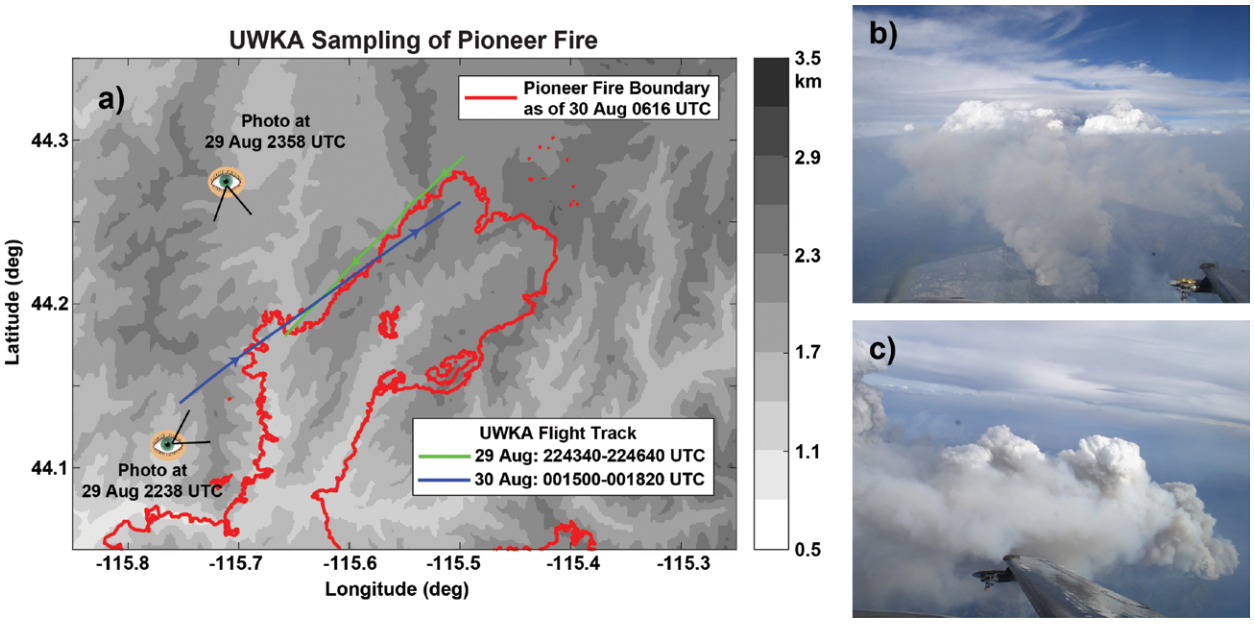

Fig. 10. (a) Topographic map of domain where the UWKA sampled the Pioneer fire. Grayscale for topography shown at right. Boundary of the Pioneer fire as of 0616 UTC 30 Aug is indicated by the red line. Green and blue lines represent the location of UWKA flight legs between 2243:40 and 2246:40 UTC 29 Aug and between 0015:00 and 0018:20 UTC 30 Aug, respectively. The positions and view angles of photographs taken from the UWKA at (b) 2238 and (c) 2358 UTC 29 Aug are indicated.

varying in elevation from ~1 to ~2.5 km MSL (Fig. 10) and vegetation dominated by coniferous trees.

A visual perspective of the Pioneer fire is provided by a photograph taken from the UWKA during the flight on 29 August (Fig. 10b). This photograph was taken at 2238 UTC and is looking toward the northeast. The photograph shows several wildfire smoke plumes ascending from the surface up to an altitude just below the aircraft flight level of ~4.9 km MSL where the background visibility improves dramatically. Above this altitude, the plumes appear to merge into a conglomeration of pyroCu clouds whose tops are well above the aircraft flight level.

In situ observations from a penetration of the pyroCu less than 10 min later (2243:40–2246:40 UTC 29 August) at the same flight level (Fig. 11) depict a very turbulent environment, especially during the first minute of this flight leg tracking from northeast to southwest (Fig. 10). Two relatively narrow updrafts peaking at just below 20 m s^{-1} were followed by a relatively wide updraft peaking at just above 35 m s^{-1} (Fig. 11a). Downdrafts of 2–4 m s^{-1} were evident on both sides of this strong updraft. There was a 3°–4°C air temperature increase from the updraft edges to the updraft peak (Fig. 11b). The relative humidity values within these updrafts were mostly below 60% with relatively small along-track variations compared to later in the leg. Corresponding cloud liquid water contents were only 10–20 mg m^{-3} (Fig. 11a), much smaller than typical cumulus clouds where such values are usually well in excess of 100 mg m^{-3} (e.g., Pruppacher and Klett 1997).

As shown in Fig. 11c, the number concentration of cloud droplets N_{CDP} was also very small (<5 cm^{-3}), while the number concentration of larger particles N_{2DP} was 0.4–0.8 L^{-1}, which is somewhat small for a cumulus cloud, but not unprecedented (e.g., Kingsmill et al. 2004). Further analysis will be required to determine whether these large particles are hydrometeors or ash particles.

A shallower plume was sampled by the WCR during a flight leg spanning 0015:00–0018:20 UTC 30 August and tracking from southwest to northeast (Fig. 10). This plume was on the southwest flank of the earlier-penetrated pyroCu. A photograph taken at 2358 UTC 29 August and looking toward the south-southeast documents its visual character (Fig. 10c). The WCR data shown in Fig. 12 use beams from both the upward- and downward-pointing antennas. Peak reflectivity values of ~−5 dBZ_e were observed near the surface between 0015:50 and 0016:40 UTC (Fig. 12a). These are areas where active fire behavior was evident on the ground. After 0016:40 UTC, the wildfire plume thickened and elevated as it was tilted downwind. Echo tops reached flight level (7.3 km MSL) by ~0017:30 UTC. Reflectivity in the elevated plume was mostly larger than −20 dBZ_e, with several pockets of ~−5 dBZ_e. The Doppler vertical velocities suggested a very turbulent character (Fig. 12b). Updrafts often exceeded 15 m s^{-1} and were

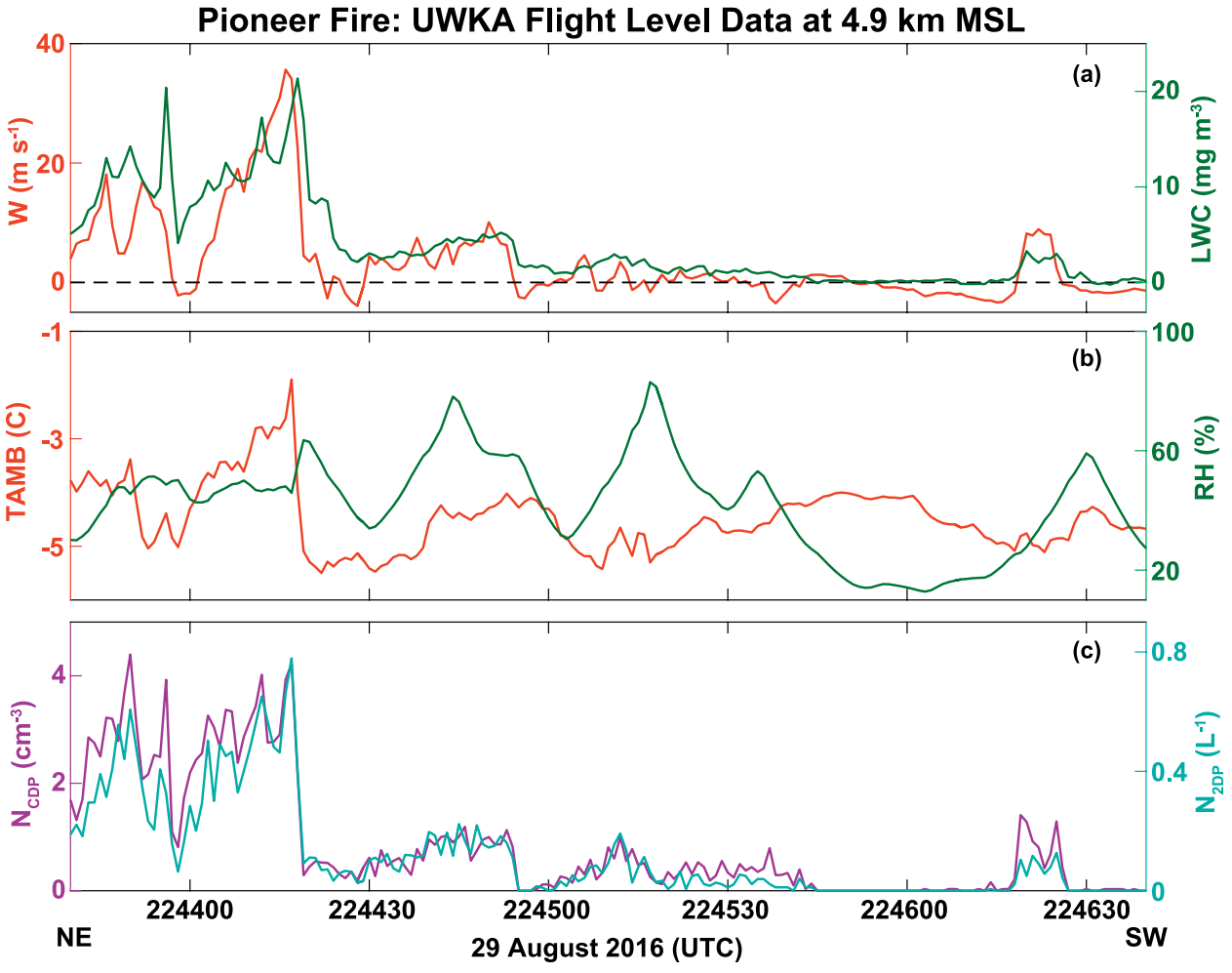

Fig. 11. In situ observations from the UWKA during a flight leg at 4.9 km MSL spanning the period 2243:40–2246:40 UTC 29 Aug and tracking from northeast to southwest (Fig. 2). (a) Vertical air velocity (red) and cloud liquid water content from the Gerber probe (green), (b) air temperature (red) and relative humidity (green), and (c) total cloud droplet concentration from the CDP probe (magenta) and total large-particle concentration from the 2DP probe (cyan).

probably closer to 20 m s^{-1} after accounting for velocity folding (WCR Nyquist velocity is 15.8 m s^{-1}). Relatively weak downdrafts are sometimes evident on the sides of strong updrafts. This is similar to the pattern observed during the pyrocumulus penetration (Fig. 11a).

Collectively, these aircraft observations amount to the first detailed collocated sampling of plume kinematics and microphysical properties, and they may provide insight for future aircraft-based observations of wildfire pyroconvective processes. Additional analyses of these data are now under way to examine, among other topics, how vertical velocity and radar reflectivity vary with height and downwind distance in the observed plumes.

SUMMARY AND FUTURE WORK. The RaDFIRE campaign was a meteorological field experiment aimed at observing and quantifying the plume dynamics and kinematics of active wildfires from within the fire environment. The campaign's deployment strategy required that the research personnel adhere to the National Incident Command protocol for fire line safety and access within the wildfire incident perimeter while making observations. The campaign employed both a rapidly deployable boundary layer profiling system, with Doppler lidar, and an aircraft equipped with a suite of in situ and remote sensors.

Significant advances from RaDFIRE presented here (and detailed in the associated RaDFIRE papers) include the following:

1) Documentation of microscale (100–1,000 m) entrainment structures in wildfire convective plumes, including the quantification of the scale

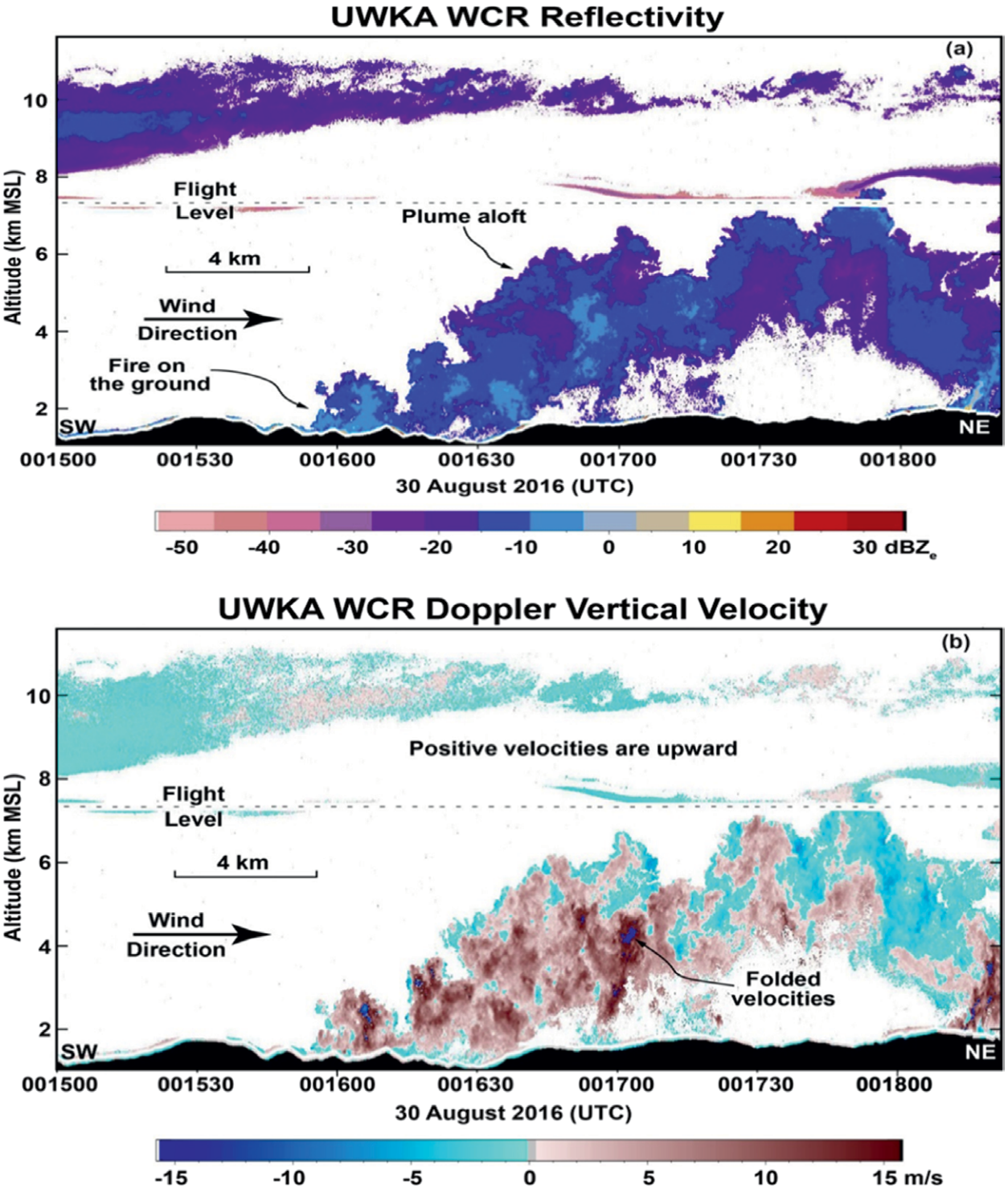

Fig. 12. WCR observations from a UWKA flight leg at 7.3 km MSL spanning 0015:00–0018:20 UTC 30 Aug and tracking from southwest to northeast (Fig. 2). Data from both the upward and downward antennas are combined in this rendering. (a) Reflectivity. (b) Doppler vertical velocity. Color bars at the bottom of both panels indicate values for their corresponding data fields. Positive Doppler vertical velocity values in (b) indicate upward motions. An abrupt change from large positive to large negative Doppler vertical velocities indicates the existence of velocity folding.

and strength of horizontal axis "ring vortices" based on direct observation.
2) Quantification of scale, strength, and evolution of vertical-axis whole-column rotation within a wildfire plume. These observations include details of the merger of two vortices, leading to vortex intensification.
3) Process-level observations of penetrative convective plumes leading to multilayered and complex smoke detrainment. These data show that wildfire plumes exhibit rapid variation in injection height at time scales of $O(10)$ min as they interact with ambient stratification and wind shear.
4) Discovery of previously unknown smoke-induced density currents forming because of reduced insolation beneath smoke layers. This finding has implications for regional-scale smoke transport predictions that are not able to resolve features on this scale arising from smoke radiative effects.
5) In situ measurements obtained by aircraft penetration into the core of a developing pyroCu, highlighting rare documentation of vigorous updrafts aloft exceeding 35 m s^{-1}.
6) Demonstration of the utility of millimeter wave radars in studying the internal structure of wildfire plumes.

In addition to these basic-science findings, another outcome of this project is the development of a dataset for the evaluation of coupled fire–atmosphere and plume-rise models. The RaDFIRE datasets are available online (www.fireweather.org/data-request/). Specifically, data from RaDFIRE provide plume observations during large active wildfires, while previously available datasets were based on small experimental fires only. Additionally, these data will inform the next generation of fire–atmosphere interaction field campaigns because of the demonstrated capabilities and performance of current observational technologies and measurement strategies.

Future campaigns will require a more comprehensive set of observations at multiple scales and from a range of platforms. For example, future deployments should incorporate high-resolution (<10 m) midinfrared (3–5 μm) observations of the fire front. This would facilitate the simultaneous observations of fire behavior characteristics and plume kinematic structures, thereby enabling the linking of plume-scale dynamics to surface fire behavior. Such fire behavior observations were not available during RaDFIRE, so our ability to assess feedbacks (i.e., two-way interactions) between the atmospheric response to the fire and the resulting surface fire behavior was limited.

In conclusion, the observations obtained from RaDFIRE will not only improve our knowledge of the dynamical structures of wildfire plumes but will also advance fire weather science beyond its historical roots of anecdotal descriptions of plume behaviors and use of indices to inform fire weather forecasters and fire behavior analysts. We hope to link these observations with next-generation coupled fire–atmosphere models. This will allow us to provide new tools for fire management to increase firefighter and community safety.

ACKNOWLEDGMENTS. The authors wish to thank the three anonymous reviewers for their comments and suggestions, which improved this manuscript. We thank Jon Contezac and Daisuke Seto for their participation in the early RaDFIRE deployments. We also wish to acknowledge and to thank the Tahoe National Forest for managing the team red card and fire line qualifications. In addition, we appreciate the efforts of the staff at the University of Wyoming King Air Research Aircraft Facility in planning for and executing the RaDFIRE aircraft campaign. This research was funded by the National Science Foundation's Physical and Dynamic Meteorology Program under Awards AGS-1151930 and AGS-1719243.

REFERENCES

Abatzoglou, J. T., and A. P. Williams, 2016: Impact of anthropogenic climate change on wildfire across western US forests. *Proc. Natl. Acad. Sci. USA*, **113**, 11 770–11 775, https://doi.org/10.1073/pnas.1607171113.

Andreae, M. O., D. Rosenfeld, P. Artaxo, A. A. Costa, G. P. Frank, K. M. Longo, and M. A. F. Silva-Dias, 2004: Smoking rain clouds over the Amazon. *Science*, **303**, 1337–1342, https://doi.org/10.1126/science.1092779.

Banta, R. M., L. D. Olivier, E. T. Holloway, R. A. Kropfli, B. W. Bartram, R. E. Cupp, and M. J. Post, 1992: Smoke-column observations from two forest fires using Doppler lidar and Doppler radar. *J. Appl. Meteor.*, **31**, 1328–1349, https://doi.org/10.1175/1520-0450(1992)031<1328:SCOFTF>2.0.CO;2.

Barbero, R., J. T. Abatzoglou, N. K. Larkin, C. A. Kolden, and B. Stocks, 2015: Climate change presents increased potential for very large fires in the contiguous United States. *Int. J. Wildland Fire*, **24**, 892–899, https://doi.org/10.1071/WF15083.

Bluestein, H. B., C. C. Weiss, and A. L. Pazmany, 2004: Doppler radar observations of dust devils in Texas. *Mon. Wea. Rev.*, **132**, 209–224, https://doi

.org/10.1175/1520-0493(2004)132<0209:DROODD>2.0.CO;2.

Brown, R. A., and V. T. Wood, 1991: On the interpretation of single-Doppler velocity patterns within severe thunderstorms. *Wea. Forecasting*, **6**, 32–48, https://doi.org/10.1175/1520-0434(1991)006<0032:OTIOSD>2.0.CO;2.

Browning, K. A., and R. Wexler, 1968: The determination of kinematic properties of a wind field using Doppler radar. *J. Appl. Meteor.*, **7**, 105–113, https://doi.org/10.1175/1520-0450(1968)007<0105:TDOKPO>2.0.CO;2.

Byram, G. M., 1959: Combustion of forest fuels. *Forest Fire: Control and Use*, K. P. Davis, Ed., McGraw-Hill, 61–89.

Church, C. R., J. T. Snow, and J. Dessens, 1980: Intense atmospheric vortices associated with a 1000 MW fire. *Bull. Amer. Meteor. Soc.*, **61**, 682–694, https://doi.org/10.1175/1520-0477(1980)061<0682:IAVAWA>2.0.CO;2.

Clark, T. L., M. A. Jenkins, J. Coen, and D. Packham, 1996: A coupled atmospheric–fire model: Convective feedback on fire line dynamics. *J. Appl. Meteor.*, **35**, 875–901, https://doi.org/10.1175/1520-0450(1996)035<0875:ACAMCF>2.0.CO;2.

Clements, C. B., and A. J. Oliphant, 2014: The California State University Mobile Atmospheric Profiling System: A facility for research and education in boundary layer meteorology. *Bull. Amer. Meteor. Soc.*, **95**, 1713–1724, https://doi.org/10.1175/BAMS-D-13-00179.1.

Coen, J., S. Mahalingam, and J. Daily, 2004: Infrared imagery of crown-fire dynamics during FROSTFIRE. *J. Appl. Meteor.*, **43**, 1241–1259, https://doi.org/10.1175/1520-0450(2004)043<1241:IIOCDD>2.0.CO;2.

Countryman, C. M., 1971: Fire whirls…why, when, and where. USFS Pacific Southwest Research Station Rep., 14 pp., www.frames.gov/documents/behaveplus/publications/Countryman_1971_FireWhirls_ocr.pdf.

Cunningham, P., S. L. Goodrick, M. Y. Hussaini, and R. R. Linn, 2005: Coherent vortical structures in numerical simulations of buoyant plumes from wildland fires. *Int. J. Wildland Fire*, **14**, 61–75, https://doi.org/10.1071/WF04044.

Damoah, R., and Coauthors, 2004: Around the world in 17 days—Hemispheric-scale transport of forest fire smoke from Russia in May 2003. *Atmos. Chem. Phys.*, **4**, 1311–1321, https://doi.org/10.5194/acp-4-1311-2004.

Dennison, P., S. Brewer, J. Arnold, and M. Moritz, 2014: Large wildfire trends in the western United States, 1984–2011. *Geophys. Res. Lett.*, **41**, 2928–2933, https://doi.org/10.1002/2014GL059576.

Flannigan, M. D., M. A. Krawchuk, W. J. de Groot, B. M. Wotton, and L. M. Gowman, 2009: Implications of changing climate for global wildland fire. *Int. J. Wildland Fire*, **18**, 483–507, https://doi.org/10.1071/WF08187.

Forthofer, J. A., and S. L. Goodrick, 2011: Vortices and wildland fire. Synthesis of knowledge of extreme fire behavior: Volume I for fire managers, Pacific Northwest Research Station General Tech. Rep. PNW-GTR-854, 89–105, www.fs.fed.us/pnw/pubs/pnw_gtr854.pdf.

Fromm, M. D., and R. Servranckx, 2003: Transport of forest fire smoke above the tropopause by supercell convection. *Geophys. Res. Lett.*, **30**, 1542, https://doi.org/10.1029/2002GL016820.

——, A. Tupper, D. Rosenfeld, R. Servranckx, and R. McRae, 2006: Violent pyro-convective storm devastates Australia's capital and pollutes the stratosphere. *Geophys. Res. Lett.*, **33**, L05815, https://doi.org/10.1029/2005GL025161.

——, D. T. Lindsey, R. Servranckx, G. Yue, T. Trickl, R. Sica, and S. Godin-Beekmann, 2010: The untold story of pyrocumulonimbus. *Bull. Amer. Meteor. Soc.*, **91**, 1193–1209, https://doi.org/10.1175/2010BAMS3004.1.

Kahn, R. A., Y. Chen, D. L. Nelson, F.-Y. Leung, Q. Li, D. J. Diner, and J. A. Logan, 2008: Wildfire smoke injection heights—Two perspectives from space. *Geophys. Res. Lett.*, **35**, L04809, https://doi.org/10.1029/2007GL032165.

Kingsmill, D. E., and Coauthors, 2004: TRMM common microphysics products: A tool for evaluating spaceborne precipitation retrieval algorithms. *J. Appl. Meteor.*, **43**, 1598–1618, https://doi.org/10.1175/JAM2151.1.

Lang, T. J., and S. A. Rutledge, 2006: Cloud-to-ground lightning downwind of the 2002 Hayman forest fire in Colorado. *Geophys. Res. Lett.*, **33**, L03804, https://doi.org/10.1029/2005GL024608.

——, ——, B. Dolan, P. Krehbiel, W. Rison, and D. T. Lindsey, 2014: Lightning in wildfire smoke plumes observed in Colorado during summer 2012. *Mon. Wea. Rev.*, **142**, 489–507, https://doi.org/10.1175/MWR-D-13-00184.1.

Lareau, N. P., and C. B. Clements, 2015: Cold smoke: Smoke-induced density currents cause unexpected smoke transport near large wildfires. *Atmos. Chem. Phys.*, **15**, 11 513–11 520, https://doi.org/10.5194/acp-15-11513-2015.

——, and ——, 2016: Environmental controls on pyrocumulus and pyrocumulonimbus initiation and

development. *Atmos. Chem. Phys.*, **16**, 4005–4022, https://doi.org/10.5194/acp-16-4005-2016.

——, and ——, 2017: The mean and turbulent properties of a wildfire convective plume. *J. Appl. Meteor. Climatol.*, **56**, 2289–2299, https://doi.org/10.1175/JAMC-D-16-0384.1.

Luderer, G., J. Trentmann, T. Winterrath, C. Textor, M. Herzog, H. F. Graf, and M. O. Andreae, 2006: Modeling of biomass smoke injection into the lower stratosphere by a large forest fire (Part II): Sensitivity studies. *Atmos. Chem. Phys.*, **6**, 5261–5277, https://doi.org/10.5194/acp-6-5261-2006.

——, ——, and M. O. Andreae, 2009: A new look at the role of fire-released moisture on the dynamics of atmospheric pyro-convection. *Int. J. Wildland Fire*, **18**, 554–562, https://doi.org/10.1071/WF07035.

McRae, D. J., and M. D. Flannigan, 1990: Development of large vortices on prescribed fires. *Can. J. For. Res.*, **20**, 1878–1887, https://doi.org/10.1139/x90-252.

Pahlow, M., J. Kleissl, M. B. Parlange, J. M. Ondov, and D. Harrison, 2005: Atmospheric boundary-layer structure observed during a haze event due to forest-fire smoke. *Bound.-Layer Meteor.*, **114**, 53–70, https://doi.org/10.1007/s10546-004-6350-z.

Pearson, G., F. Davies, and C. Collier, 2009: An analysis of the performance of the UFAM pulsed Doppler lidar for observing the boundary layer. *J. Atmos. Oceanic Technol.*, **26**, 240–250, https://doi.org/10.1175/2008JTECHA1128.1.

Penner, J. E., R. E. Dickinson, and C. S. O'Neill, 1992: Effects of aerosol from biomass burning on the global radiation budget. *Science*, **256**, 1432–1434, https://doi.org/10.1126/science.256.5062.1432.

Peterson, D. A., E. J. Hyer, J. R. Campbell, M. D. Fromm, J. W. Hair, C. F. Butler, and M. A. Fenn, 2015: The 2013 Rim fire: Implications for predicting extreme fire spread, pyroconvection, and smoke emissions. *Bull. Amer. Meteor. Soc.*, **96**, 229–247, https://doi.org/10.1175/BAMS-D-14-00060.1.

——, ——, ——, J. E. Solbrig, and M. D. Fromm, 2017: A conceptual model for development of intense pyrocumulonimbus in western North America. *Mon. Wea. Rev.*, **145**, 2235–2255, https://doi.org/10.1175/MWR-D-16-0232.1.

Potter, B. E., 2012: Atmospheric interactions with wildland fire behavior—II. Plume and vortex dynamics. *Int. J. Wildland Fire*, **21**, 802–871, https://doi.org/10.1071/WF11129.

Pruppacher, H. R., and J. D. Klett, 1997: *Microphysics of Clouds and Precipitation*. Kluwer Academic, 954 pp.

Radke, L. F., J. H. Lyons, P. V. Hobbs, D. A. Hegg, D. V. Sandberg, and D. E. Ward, 1990: Airborne monitoring and smoke characterization of prescribed fires on forest lands in western Washington and Oregon. Pacific Northwest Research Station General Tech. Rep. PNW-GTR-251, 81 pp., https://doi.org/10.2737/PNW-GTR-251.

——, and Coauthors, 1991: Particulate and trace gas emissions from large biomass fires in North America. *Global Biomass Burning: Atmospheric, Climatic, and Biospheric Implications*, J. S. Levine, Ed., MIT Press, 209–224.

Reid, J. S., and P. V. Hobbs, 1998: Physical and optical properties of young smoke from individual biomass fires in Brazil. *J. Geophys. Res.*, **103**, 32 013–32 030, https://doi.org/10.1029/98JD00159.

——, R. Koppmann, T. F. Eck, and D. P. Eleuterio, 2005: A review of biomass burning emissions part II: Intensive physical properties of biomass burning particles. *Atmos. Chem. Phys.*, **5**, 799–825, https://doi.org/10.5194/acp-5-799-2005.

Robock, A., 1988: Enhancement of surface cooling due to forest fire smoke. *Science*, **242**, 911–913, https://doi.org/10.1126/science.242.4880.911.

——, 1991: Surface cooling due to forest fire smoke. *J. Geophys. Res.*, **96**, 20 869–20 878, https://doi.org/10.1029/91JD02043.

Rosenfeld, D., M. Fromm, J. Trentmann, G. Luderer, M. O. Andreae, and R. Servranckx, 2007: The Chisholm firestorm: Observed microstructure, precipitation and lightning activity of a pyro-cumulonimbus. *Atmos. Chem. Phys.*, **7**, 645–659, https://doi.org/10.5194/acp-7-645-2007.

Rothermel, R. C., 1991: Predicting behavior and size of crown fires in the northern Rocky Mountains. USDA Research Paper RP-438, 46 pp.

Segal, M., and R. W. Arritt, 1992: Nonclassical mesoscale circulations caused by surface sensible heat-flux gradients. *Bull. Amer. Meteor. Soc.*, **73**, 1593–1604, https://doi.org/10.1175/1520-0477(1992)073<1593:NMCCBS>2.0.CO;2.

Seto, D., and C. B. Clements, 2011: Fire whirl evolution observed during a valley wind-sea breeze reversal. *J. Combust.*, **2011**, 569475, https://doi.org/10.1155/2011/569475.

Simpson, J. E., 1997: *Gravity Currents: In the Environment and the Laboratory*. Cambridge University Press, 244 pp.

Trentmann, J., and Coauthors, 2006: Modeling of biomass smoke injection into the lower stratosphere by a large forest fire (Part I): Reference simulation. *Atmos. Chem. Phys.*, **6**, 5247–5260, https://doi.org/10.5194/acp-6-5247-2006.

Umscheid, M. E., J. P. Monteverdi, and J. M. Davies, 2006: Photographs and analysis of an unusually large

and long-lived firewhirl. *Electron. J. Severe Storms Meteor.*, **1** (2), www.ejssm.org/ojs/index.php/ejssm/article/viewArticle/6/11.

Val Martin, M., J. A. Logan, R. A. Kahn, F.-Y. Leung, D. L. Nelson, and D. J. Diner, 2010: Smoke injection heights from fires in North America: Analysis of 5 years of satellite observations. *Atmos. Chem. Phys.*, **10**, 1491–1510, https://doi.org/10.5194/acp-10-1491-2010.

——, R. A. Kahn, J. A. Logan, R. Paugam, M. Wooster, and C. Ichoku, 2012: Space-based observational constraints for 1-D plume rise models. *J. Geophys. Res.*, **117**, D22204, https://doi.org/10.1029/2012JD018370.

Viegas, D. X., 1998: Convective processes in forest fires. *Buoyant Convection in Geophysical Flows*, E. J. Plate et al., Eds., Springer, 401–420.

Wang, Y., and B. Geerts, 2015: Vertical-plane dual-Doppler radar observations of cumulus toroidal circulations. *J. Appl. Meteor. Climatol.*, **54**, 2009–2026, https://doi.org/10.1175/JAMC-D-14-0252.1.

Wang, Z., and Coauthors, 2012: Single aircraft integration of remote sensing and in situ sampling for the study of cloud microphysics and dynamics. *Bull. Amer. Meteor. Soc.*, **93**, 653–668, https://doi.org/10.1175/BAMS-D-11-00044.1.

Weil, J. C., 1988: Plume rise. *Lectures on Air Pollution Modeling*, A. Venkatram, Ed., Amer. Meteor. Soc., 119–166.

Werth, P. A., 2011: Critical fire weather patterns. Synthesis of knowledge of extreme fire behavior: Volume I for fire managers, Pacific Northwest Research Station General Tech. Rep. PNW-GTR-854, 25–48, www.fs.fed.us/pnw/pubs/pnw_gtr854.pdf.

Westerling, A. L., H. G. Hidalgo, D. R. Cayan, and T. W. Swetnam, 2006: Warming and earlier spring increase western U.S. forest wildfire activity. *Science*, **313**, 940–943, https://doi.org/10.1126/science.1128834.